We are IntechOpen,
the world's leading publisher of Open Access books
Built by scientists, for scientists

4,800
Open access books available

122,000
International authors and editors

135M
Downloads

154
Countries delivered to

Our authors are among the

TOP 1%
most cited scientists

12.2%
Contributors from top 500 universities

BOOK CITATION INDEX
CLARIVATE ANALYTICS
INDEXED

WEB OF SCIENCE™

Selection of our books indexed in the Book Citation Index
in Web of Science™ Core Collection (BKCI)

Interested in publishing with us?
Contact book.department@intechopen.com

Numbers displayed above are based on latest data collected.
For more information visit www.intechopen.com

Holography at the Nano Level With Visible Light Wavelengths

Cesar A. Sciammarella, Luciano Lamberti and
Federico M. Sciammarella

1. Introduction

Microscopy was invented in the 17th century, and after four centuries the methodology to get information at increasingly small distances has become a complex multidisciplinary science. Abbe, towards the middle of 1870s, introduced the fundamental idea that, due to the wave nature of light, the resolving power of a microscope was constrained by its angular aperture that limited the number of components of an image. Almost at the same time, Lord Rayleigh introduced his criterion based on the work of Airy dealing with the optical astronomy problem of the separation of two stars.

An optical method to overcome the classical limits of resolution was initiated by Toraldo di Francia in the late 1940s, about 65 years ago, utilizing evanescent fields [1]. The motivation came from the solutions of the Maxwell's equations and the theory of antennae. He foresaw the possibility of increasing resolution to a limit only constrained by the indetermination principle that connects the energy available in an observation process to the spatial resolution that can be achieved.

The authors [2], following this line of research, reported in 2006 the successful detection of information well beyond the optical resolution limit getting down to 4 nm, that is 1/79 of the classical resolution limit $\lambda/2$. The experiments conducted by the authors yielded later on very important developments that connect super-resolution with an optical method very similar in its formalism to Fourier transform holography.

This chapter will cover the following topics: 1) basic definitions on evanescent fields and fundamental relationships; 2) generation of super-oscillatory fields; 3) processes involved in the transformation of super-resolution near fields, that are well known and extensively re-

searched, into propagating fields that can be observed in the far field; 4) similarity between the observed images and FT holography but in the context of a different type of diffraction effect; 5) extraction of 3-D information from the 2-D image of the pseudo-FT hologram; 6) digital reconstruction of the pseudo-FT holograms of simple objects such as prismatic nano-crystals and nano-spheres; 7) verification of the obtained results; 8) numerical issues entailed by the reconstruction process; 9) discussion and conclusions.

2. Evanescent fields

2.1. Evanescent wave's solution of Maxwell equations

Let us consider the solution of the Maxwell equations for planar propagating waves, the vectorial Helmholtz equation. By taking an exponential function as a solution of the Maxwell equations of the form $\exp(i\omega t)$ one gets the following vector equation:

$$(\nabla^2 + \omega^2 \mu_0 \varepsilon_0)\left\{ \begin{array}{c} \vec{E} \\ \vec{B} \end{array} \right\} = 0 \tag{1}$$

The electric and the magnetic field vectors $\vec{E}$ and $\vec{B}$ satisfy the above equation (1). The notation ∇^2 indicates the Laplace operator, $\omega=2\pi f=2\pi/T$ is the temporal angular period, ε_o and μ_o are the permittivity and permeability of vacuum, respectively. By introducing the argument $\exp(k \bullet \vec{r} - i\omega t)$, the periodicity in space is included in the wave solution. The quantity k is the wave number $2\pi/\lambda$, $\vec{r}$ is the position vector. The vector $\vec{r}$ is characterized for a plane wave by the equation, $\vec{r} = r(\alpha \, i + \beta \, j + \gamma \, k)$, where α, β, γ are the direction cosines of the considered vector. A general solution of Eq. (1) is possible, by assuming that α, β, γ are complex quantities that have real and imaginary components. By defining:

$$\begin{aligned} \alpha &= a_1 + i\,a_2 \\ \beta &= b_1 + i\,b_2 \\ \gamma &= c_1 + i\,c_2 \end{aligned} \tag{2}$$

the dotted $\vec{k} \bullet \vec{r}$ product gives:

$$\vec{k} \bullet \vec{r} = k\left[-(a_2 x + b_2 y + c_2 z) + i(a_1 x + b_1 y + c_1 z) \right] \tag{3}$$

Let us apply the above derivations to the problem of total reflection, Figure 1. For simplicity, the analysis is reduced to a two dimensional problem, by analyzing the process in the inci-

dence plane of a propagating beam from medium 1 to medium 2 such that $n_1 > n_2$, where n_1 and n_2 are the indices of refraction of the two media. Considering the total internal reflection condition, introducing the refraction equation and calling θ_i the angle of incidence and θ_t the angle of the transmitted light one arrives to the following conclusions:

1. There is a surface wave that propagates in the X-direction as a plane wave.

2. The planes of constant phase and constant amplitude are orthogonal to each other.

3. The electromagnetic field penetrates the second medium but decays very rapidly in the Z-direction.

4. If the electric vector is contained in the plane of incidence, the evanescent field electric vector becomes elliptically polarized in the plane of incidence, (p-polarization).

5. If the electric vector is orthogonal to the plane of incidence (s-polarization), the polarization does not experience changes.

6. If one computes the Poynting vector of the field on the upper half of the plane, one concludes that no energy is transmitted to the second medium.

7. Computing the modulus of the component k_z of the $\vec{k}$ vector (see Figure 1b) one arrives to the conclusion that this component oscillates with spatial frequencies $2\pi/\lambda_e$, much higher than the spatial oscillation of all ordinary electromagnetic waves. Berry [3] showed that such a field is a super-oscillatory field that through scattering in a medium can be transformed into an actual near field. This approach leads to the near-field microscopic detection that is well documented in the literature.
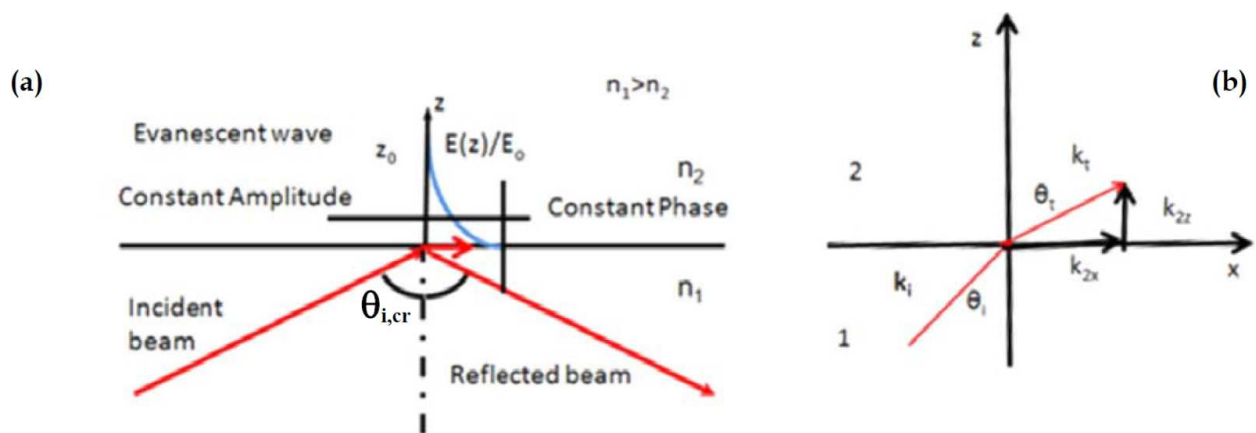

Figure 1. Characteristics of evanescent field: (a) Orthogonality of the vectors of constant phase and constant amplitude and exponential decay of the vector amplitude in the z-direction; (b) Resultant **k_t** vector penetrating in the second medium.

3. Improvement of the optical resolution of an optical instrument via evanescent illumination

Scanning probe devices are currently utilized to collect local information on the electromagnetic field lying near a surface of different geometrical configurations. Over the past decade, optical experiments based on near field observations have been developed via scanning probe devices. These experiments demonstrated the actual realization of optical resolutions well beyond the classical $\lambda/2$ limit mentioned in the Introduction section. In this work, we are concerned with the problem of how the electromagnetic field interacts with nano-sized objects producing propagating light waves capable of carrying information generated in the near field up to the far field where this information is retrieved. This phenomenon involves in the near field what is called in the literature "confined electromagnetic fields" since the near field electromagnetic fields exist in nano-objects that are smaller than the wavelength of the illuminating light.

Reference [4] addresses the relationship between the field generated by the evanescent illumination in the case of an array of objects similar to the one depicted in Figure 2a, a prismatic nano-crystal lying on a microscopic slide. Figure 2b shows the field resulting from TM polarization for such an array, the k_x component is a super-oscillatory component. The objects are 25 nm tall and the field is represented at 30 nm from the plane x-y; the field resembles the geometry of the objects. However, the TE polarization provides patterns that indicate the edges of the protrusions. The results provided in [4] indicate the increasing resolution of the field in following the shape of the objects, as the objects become sub-wavelength in dimensions and this field has its source of energy in the electro-magnetic field created by the evanescent waves.
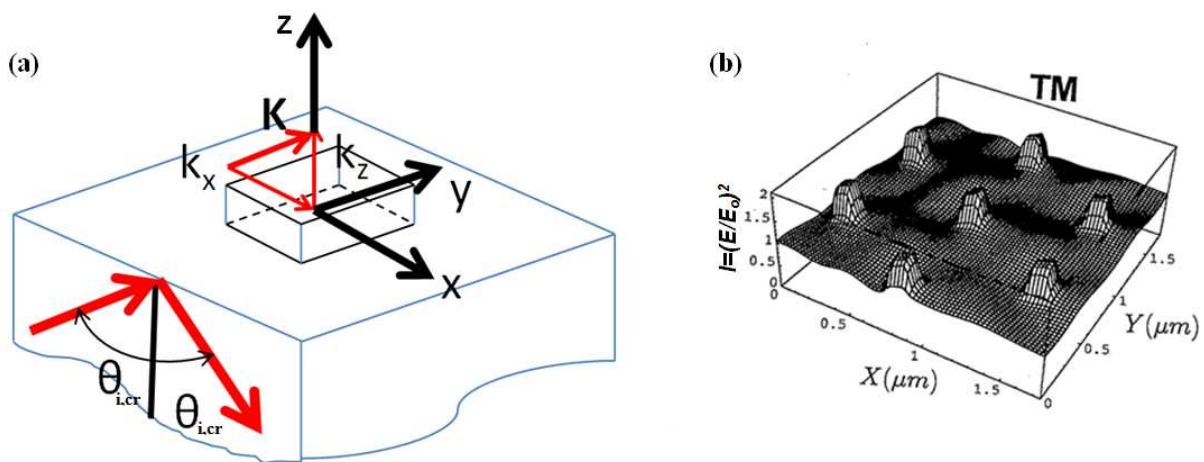

Figure 2. (a) Example of one of the observed objects in this work, a prismatic nano-crystal lying on a microscope slide. The k vector of the propagating wave front and its components are indicated. The object dimensions are sub-wavelength, of the order of magnitude close to $\lambda/10$; (b) Electric field intensity lines in the neighborhood of array of objects similar to the one depicted in Figure 2a.

Having summarized the basic properties of the evanescent waves, and from reference [4] concluded that the presence of a dielectric object in the evanescent field produces a scattering field that when the dimensions of the object are sub-wavelength resembles the object's geometry, it is necessary to look further to the relationship existing between evanescent waves and super-resolution. The presence of super-oscillations in the near field was postulated by Toraldo di Francia [1,5]. A formal approach relating evanescent fields and super-resolution is due to Vigoureux [6]. It is interesting to look back to this argument for the implications that it has in the retrieval of information from the geometry of the near field. The starting point of the argument is the uncertainty principle of FT. From the uncertainty principle of FT [7] applied in the x-direction, and applied to the pair of complementary quantities position and wave vector component, Δx and Δk_x respectively, Vigoreux shows that the uncertainty principle leads to the inequality,

$$\Delta x \, \Delta k_x > 2\pi \tag{4}$$

From the above inequality, one can conclude that to obtain the smallest spatial resolution Δx it is necessary that the interval Δk_x must be as large as possible. The classical solution of the Maxwell equation for propagating waves in vacuum (approximately in air) provides a limit. This limit can be computed by observing that the limit imposed by the condition of total reflection from a material of index of refraction n with respect to vacuum gives values of $k_x = -\omega/c, +\omega/c = -2\pi/\lambda, +2\pi/\lambda$, resulting in a $\Delta k_x = 4\pi/\lambda$. Replacing this value in Eq. (4) one obtains $\Delta x = \lambda/2$, which brings the Rayleigh limit.

If we consider now evanescent waves as sources of electromagnetic energy capable to excite a medium and create super-oscillating fields, the values Δk_x are no longer limited to the above mentioned interval. When the diffracted waves corresponding to the plane wave fronts with real direction cosines arrive to the limit $\lambda/2$, the solutions of the evanescent plane wave fronts with complex direction cosines add new frequencies to the spectrum. In order to estimate the actual Δk_x interval, let us introduce a simple mathematical argument that will allow making an estimate of the values of k_x for evanescent waves without a more extensive derivation.

A one-dimension model is sufficient for this purpose. By utilizing the scalar theory of light wave propagation, one can start from the Fourier solution of Maxwell equations:

$$E(x, \tau) = \frac{1}{\sqrt{2\pi}} \int_{-\infty}^{+\infty} E(k) e^{ikx - i\omega(k)\tau} \, dk \tag{5}$$

where: $E(x,\tau)$ is the scalar representation of the propagating electromagnetic field; x is the spatial coordinate; τ is the time; $E(k)$ is the amplitude of the electric field of angular frequency $\omega(k)$. $E(k)$ provides the linear superposition of the different waves that propagate and can be expressed as $E(k) = \sqrt{2\pi} \, \delta(k - k_o)$, where $\delta(k - k_o)$ is the Dirac's delta function.

E(k) corresponds to the monochromatic wave $E(x,\tau)=e^{ikx-i\omega(k)\tau}$. If one considers a spatial pulse of finite length L_{wt} at the time $\tau=0$, $E(x,0)$ represents a finite wave-train of length L_{wt}, where E(k) is not a delta function but a function that contains an angular spread Δk. The dimension of L_{wt} depends on the size of the analyzed object. If L_{wt} and Δk are defined as the RMS deviations from the corresponding average values $|E(x,0)|^2$ and $|E(k)|^2$ evaluated in terms of intensities, it can be shown that $L_{wt} \bullet \Delta k \geq 1/2$. If L_{wt} is very small, the spread of wave numbers must be large. Hence, there is a quite different scenario with respect to the classical context where the length L_{wt} is large compared to the wavelength of light. Again, there will be super-oscillatory waves. A nanometric object will support super-oscillatory evanescent waves and the spectrum of diffraction will be wider as the dimension of the object becomes smaller.

Some conclusions can be drawn from the above derivations. The interval of Δk_x is no longer limited to $-2\pi/\lambda \leq k_x \leq +2\pi/\lambda$, but can be extended to $2\pi/\lambda \leq k_x \leq +\infty$. There are practical limitations but one can obtain evanescent waves with increasing k_x and accordingly increasing the interval Δk_x. The resolution can be increased well beyond the Rayleigh limit. However, as the values of Δk_x increase, the values of Δk_z are reduced since the sum of the two components is the vector $\vec{k_t}$: therefore, as Δk_z decreases, the depth of penetration of the field in the second medium is reduced. Hence, the high frequency components of the observed objects that are located at the interface of the plane of separation of the two media remain limited at distances very close to the separation plane. All the above derivations are in agreement with the near field microscopy methods. Another important point that can be extracted from the above considerations is the following. If we consider the case of a single element shown in Figure 2, one single beam will generate a single k_x and hence the resolution will be limited to this particular value. To increase the Δk_x it will be necessary to increase the angle θ shown in Figure 2a. A practical way to achieve this objective will be described in what follows.

In summary, objects as the one depicted in Figure 2 supported by a surface where an evanescent wave is propagating generate confined electromagnetic fields. Results presented in [4] show that if the dimensions of the surface elements are varied, the interaction between the objects and the electromagnetic field changes. Larger objects produce both real waves with real direction cosines and evanescent waves with imaginary direction cosines. The evanescent component becomes predominant as the dimensions of the object are reduced and the confinement is increased. Increasing confinements lead to fields that, depending on their state of polarization, resemble the geometry of the objects.

4. Generation of multiple k-vectors evanescent fields with TE and TM polarizations

In order to understand the generation of multiple **k** vectors with TE and TM illuminations, we need to introduce the optical set up utilized to perform the observations. Following the classical arrangement of total internal reflection (see Figure 3), a helium-neon (He-Ne) laser

beam with nominal wavelength 632.8 nm sends a beam in the direction of the normal of a penta-prism designed to produce limit angle illumination at the interface between a microscope slide and a saline solution of sodium-chloride contained in a small cell.

The prism is supported in the platina of a microscope utilized to record the images of the observed objects. Inside the cell filled with the NaCl solution there is a polystyrene microsphere of 6 μm diameter. The microsphere is fixed to the face of the slide through chemical treatment of the contact surface in order to avoid Brownian motions. The polystyrene sphere plays the role of a relay lens that collects the light wave fronts generated by the observed nano-sized objects resting on the microscope slide. Table 1 provides information on the spherical particle and the index of refraction of the saline solution.

The microscope has a NA=0.95. Two CCD sensors are attached to the microscope. A monochromatic CCD is a square pixel camera with 1600 x 1152 pixels. At a second port, a color camera records color images. The analysis of the image recorded in the experiment is performed with the Holo Moiré Strain Analyzer software (HoloStrain™) [8], developed by C.A. Sciammarella and his collaborators.
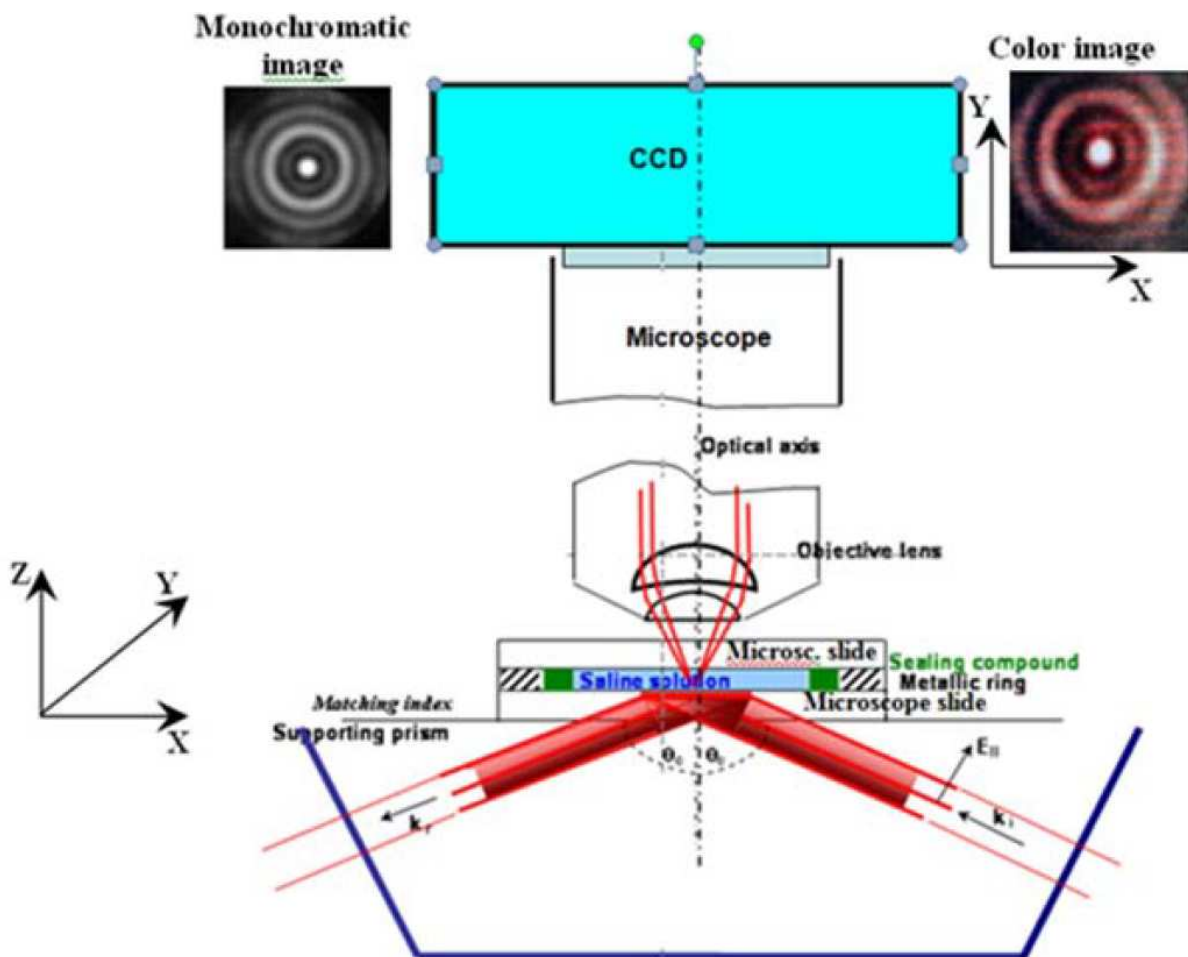

Figure 3. Optical set up utilized to observe the nano-objects.

Parameter	Value	Note
Polystyrene microsphere diameter D_{sph}	6 ± 0.042 μm	Tolerance specified by the manufacturer
Refraction index of polystyrene sphere n_p	1.57 ± 0.01	Value specified by the manufacturer
Refraction index of saline solution n_{so}	1.36	Computed from NaCl concentration for λ=590 nm

Table 1. Details on polystyrene microsphere and saline solution.

It will be shown that the above described optical set up provides the multiple **k** vectors. The initial polarization as indicated in Figure 2 is TE. Multiple illumination beams travelling in the penta-prism are generated by the residual stresses in the outer layers of the prism that hence acts as a volume grating. In Refs. [9,10], there are two attempts to analyze the formation of interference fringes originated by evanescent illumination in presence of residual stresses on glass surfaces. Before proceeding to further analyze generation of multiple **k** plane waves, some properties of the scattered light must be recalled.
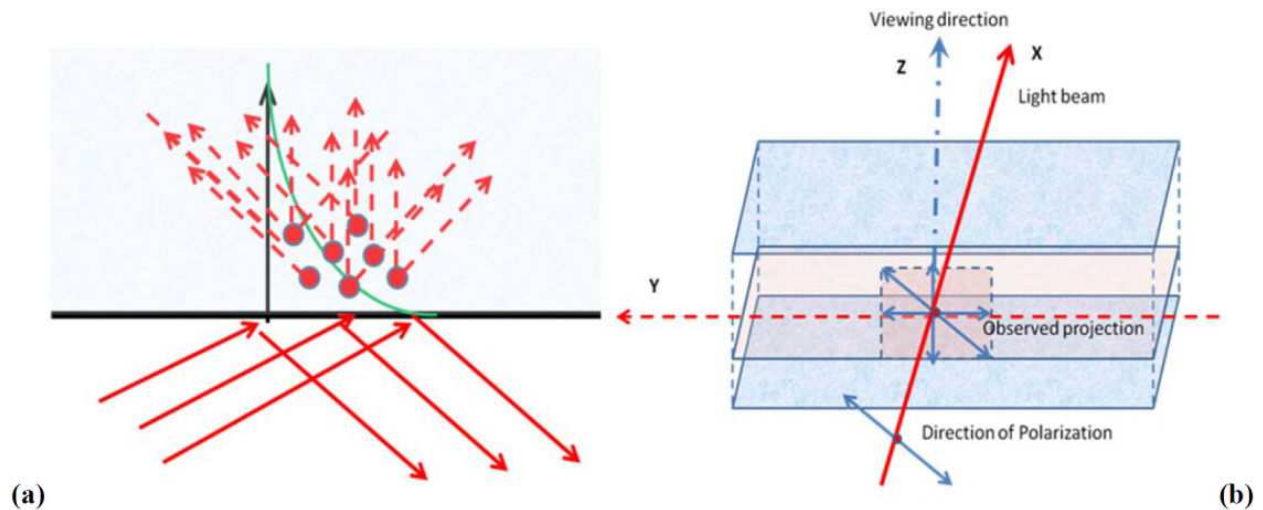

Figure 4. (a) Illustration of the effect of the electromagnetic evanescent field penetrating into a dielectric medium; (b) Observation of events that take place in the X-Y plane in the direction perpendicular to a scattered light beam propagating in the dielectric medium.

Figure 4a illustrates the scattering (diffraction effect) of the evanescent field entering in a dielectric medium. The actual problem is very complex [11] and the main properties of interest for the present derivation will be summarized in what follows. At this point, an additional element must be introduced that has to do with the recording of the information generated in the X-Y plane. Because the observation of the field is done in the Z-direction (see Figure 4b), it is necessary to have a mechanism that transforms the changes taking place in the X-Y plane into observable quantities in the Z-direction. The process of light scattering achieves this objective. The observer sees the projection of the vector $\vec{E}$ in the direction perpendicular to the observation vector. If non-polarized light enters the medium, the electromagnetic field becomes polarized. In Figure 4b it is shown the case of plane-polarized light entering the scattering medium: the observer sees the projected polarization vector; this conclusion ap-

plies to all types of polarization. Another important property that is relevant for the present analysis is the phenomenon of scattered light photoelasticity. In a stressed medium and observing the medium in the direction perpendicular to the propagating beam, fringes will be observed that are given by the following equation,

$$d\delta_s / dx = C(\sigma_1^s - \sigma_2^s) \tag{6}$$

where: σ_1^s and σ_2^s are the principal secondary stresses acting in the plane of the propagating beam, C is the photoelastic constant expressed in m^2/N, $d\delta_s/dx$ is the gradient of the retardation in the X-direction. The existence of these fringes on the surface of artificially birefringent media is a well known phenomenon. The existence of scattered light fringes on the surfaces has been known for a very long time, and has been used to measure residual stresses in glass surfaces since the early 1960s [12–15]. A comprehensive analysis of the formation of the fringes can be found in [15]. An important fact pointed out in [15] is that the observed fringes are multiple order interference fringes and the frequency composition depends on the profile of the residual stresses in the neighborhood of the surface.
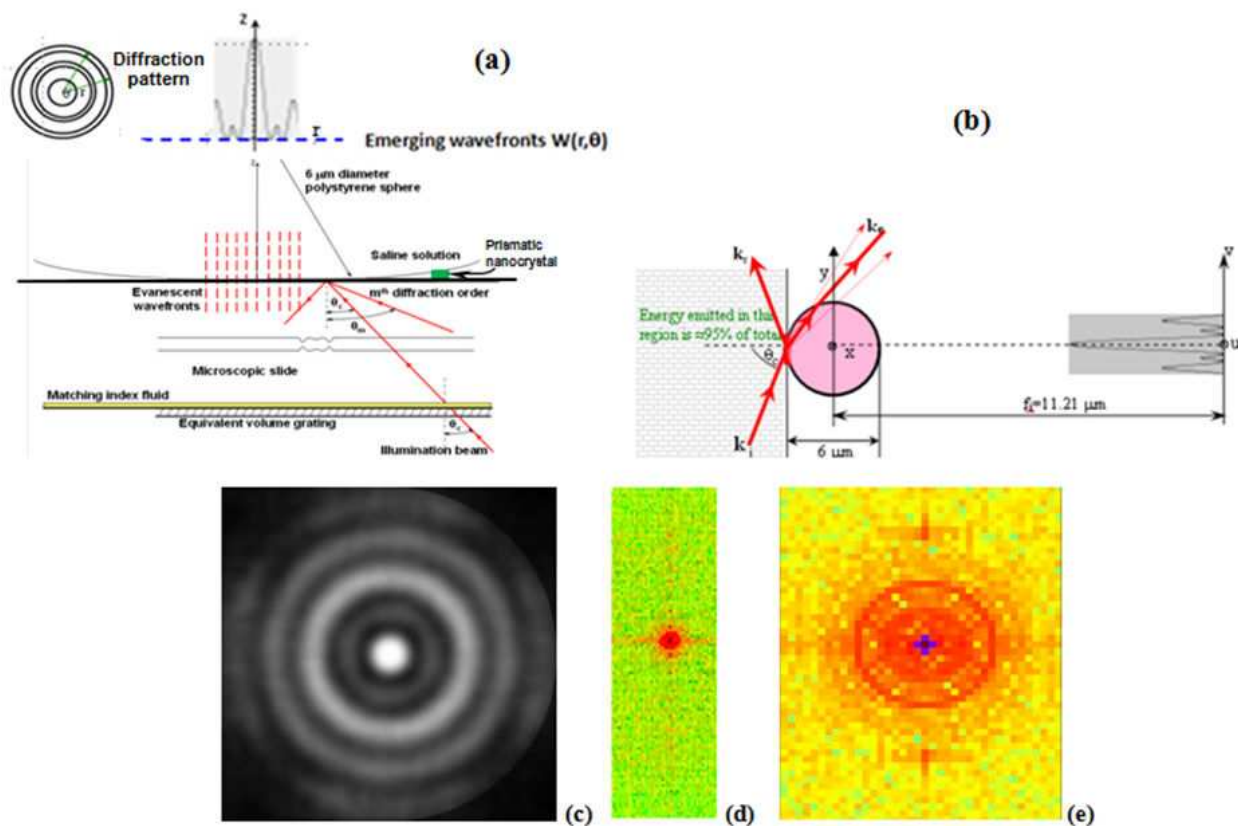

Figure 5. (a) Overall illustration of the set up geometry involved in the formation of observed fringes; prismatic nanocrystals lay on the microscope slide; (b) Relay lens (microsphere) illuminated by the evanescent field and diffraction pattern of the lens formed at the focal distance of the lens; (c) Observed pattern of the relay lens (microsphere) filtered to show average intensities; (d) FT pattern of the observed image; (e) Enlarged central portion of the FT pattern shown in Figure 5d.

Figure 5a shows the laser light incident at the interface between the upper face of the prism and the microscope slide that forms the lower face of the small cell containing the polystyrene microsphere that acts as a relay lens. The stressed upper layer of the prism is a volume diffraction grating that produces multiple diffraction orders. Between the prism and the microscopic slide there is a matching index fluid that insures the continuity of the optical path of the incident beams in the interface prism-microscope slide. In correspondence of the equivalent volume grating, different wave fronts emerge and continue their path to the interface microscope slide-saline solution where the evanescent field is generated. Because of the birefringence two wave fronts emerge from the equivalent grating: the ordinary and the extraordinary beams that have orthogonal polarizations. Figure 5b shows the interface of the microscope slide and the arriving illuminating laser beam. The total reflection at this interface produces the evanescent field that produces the diffraction pattern of the spherical relay lens. Figure 5c shows the diffraction pattern of the sphere that has been filtered to extract the pattern intensity distribution. Figure 5d shows the FT of the diffraction pattern of the captured image. Figure 5e shows the enlarged central part of the FT of the diffraction pattern.

An analysis of the pattern shown in Figure 5c that deals with its formation has been presented in [16,17]. The obtained results have been confirmed by a formal solution of the problem of a sphere illuminated by evanescent illumination utilizing Debaye's potentials [18]. There are two important aspects of the analysis of the formation of the sphere's diffraction pattern to be highlighted. The results presented in references [16–18] through the scale of the fringes diffraction pattern confirm the assumption that the microscope is focused at the focal plane of the sphere. The results also support the model of the interface between the prism and the microscope glass slide acting as a diffraction grating that causes the impinging beam to split into different diffraction orders. In [16,17] utilizing the plane wave complex solutions of the Maxwell equations and applying a method outlined by Toraldo di Francia in [5] the following equation was derived:

$$\sin\theta_n = \frac{n_o}{n_{so}}\sin\theta_i + \frac{\lambda}{n_{so}\dfrac{p_o}{N}} \tag{7}$$

In equation (7), θ_i is the angle of incidence of the laser beam shown in Figure 2; n_{so} is the index of refraction of the saline solution (see Table 1); n_o is the index of the refraction of the microscope slide (see Table 2 and Figure 8); θ_n is the angle of the evanescent diffraction order N; λ is the actual wavelength of the light generating the plane evanescent wave fronts; the integers $N_o=1,2,3,\dots$ represent the fraction of the wavelength generating interference fringes. Upon total reflection, Eq. (7) can be rewritten as:

$$\sin\theta_n = 1 + \sin\theta_{en} \tag{8}$$

The value of the first term is equal to one because it corresponds to the total reflection of the beam. We introduce the notation $\sin\theta_{en}$ for the second term where the subscript "en" indicates the evanescent order N. With this notation,

$$\sin\theta_{en} = \frac{\lambda}{n_{so}\dfrac{p_o}{N}} \tag{9}$$

By defining the effective wavelength,

$$\lambda_e = \frac{\lambda}{n_{so}} \tag{10}$$

and the pitch corresponding to the Nth evanescent order, we get

$$p_n = \frac{p_o}{N} \tag{11}$$

Using the notation reported above, equation (9) can be written as:

$$\sin\theta_{en} = \frac{\lambda_e}{p_n} \tag{12}$$

The results of the model including equations (7-12) are plotted in Figure 6a for two families of rectilinear fringes observed in the FT pattern shown in Figure 5d. Point and triangle dots in the figure correspond to order values measured experimentally. The continuous curves represent the correlation between the experimental results and the theoretical model.

Figure 6b shows an excellent correlation between the fringe spacing obtained by dividing the whole field of view of the recorded image by the order and Eq. (11). The values of the resulting hyperbolic laws written in Figure 6b provide, for each order N, the pitch p_n of the equivalent grating pitch for the corresponding order as a function of the fundamental pitch p_o of each of the two families of rectilinear fringes generated by the p-polarized and the s-polarized waves, respectively.

There is a third family of fringes that has been detected in Figure 5d and it is shown in Figure 7. Because the microscope slide acts like an interferometer, it is possible to observe two families of fringes of absolute retardation and the third family of fringes of relative retardation. Figure 7 shows that the fundamental spatial frequency of the fringes of relative retardation is equal to the difference between the fundamental spatial frequencies of the fringes of absolute retardation: that is, $p_3 = p_1 - p_2$. Replacing values, one gets: $p_3 = (3.356 - 2.238)$ μm $= 1.118$ μm.
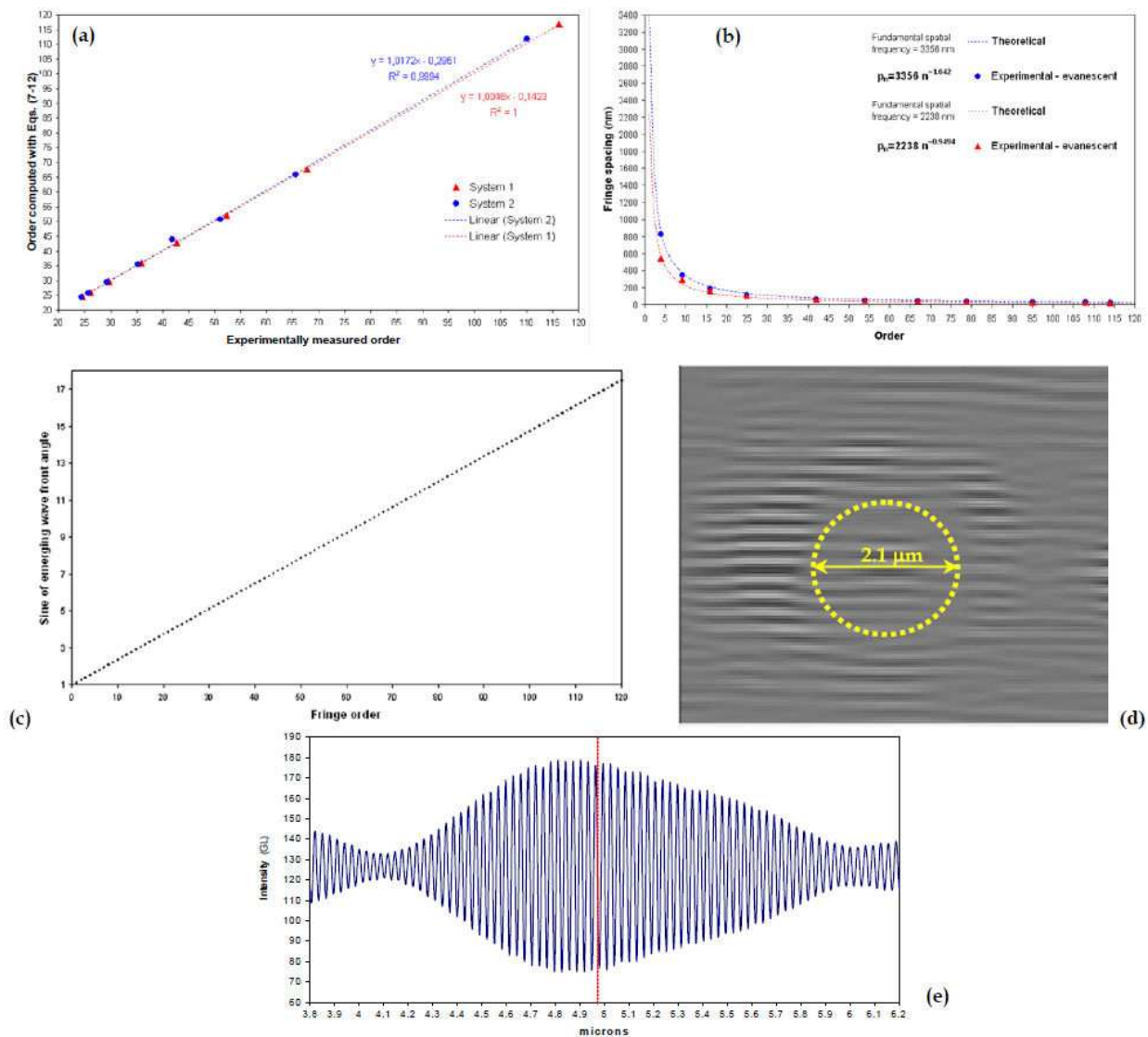
Figure 6. (a) Correlation between experimental fringe order values extracted from Figure 5d and theoretical values computed with Eqs. (7-12); (b) Two families of fringes can be extracted from the FT in Figure 5d; (c) Plot of the complex sine vs. fringe order according to Eq. (7); (d) Fringes observed in the image field of the sphere: they are modulated by the microsphere diffraction pattern (the dotted circle of diameter 2.1 μm represents the first dark ring in the diffraction pattern shown in Figure 5c; (e) Cross-section of the fringe pattern of Figure 6d.

The rectilinear fringes are modulated by the diffraction pattern of the particle (see Figure 6d). Figure 6e shows the cross-section of these fringes in the region corresponding to the central crown of the diffraction pattern of the sphere. In this cross-section, it is possible to observe the modulation of a system of parallel fringes produced by the presence of the polystyrene microsphere.

Figure 8 shows the wave fronts involved in the formation of the observed fringes. The illuminating beam as it arrives at the interface between the prism and the microscope slide is diffracted because of the residual stresses existing in the surface layer of the prism. At the interface prism-microscope slide, the incident beam is diffracted by the residual stresses that act as a dif-

fraction grating. In order to analyze the effect of the diffraction, it must be realized that due to the birefringence of the upper layer of the prism the incident beam is split into two beams: (i) the ordinary beam that has an index of refraction n_{sp} very close to the glass of the prism and also to the microscope slide; (ii) the extraordinary beam that has an index of refraction lower than the ordinary beam because birefringent glass is equivalent to a negative crystal. Both beams are orthogonally polarized hence they cannot interfere with each other. Consequently two zero order beams propagate in the slide with slightly different directions.
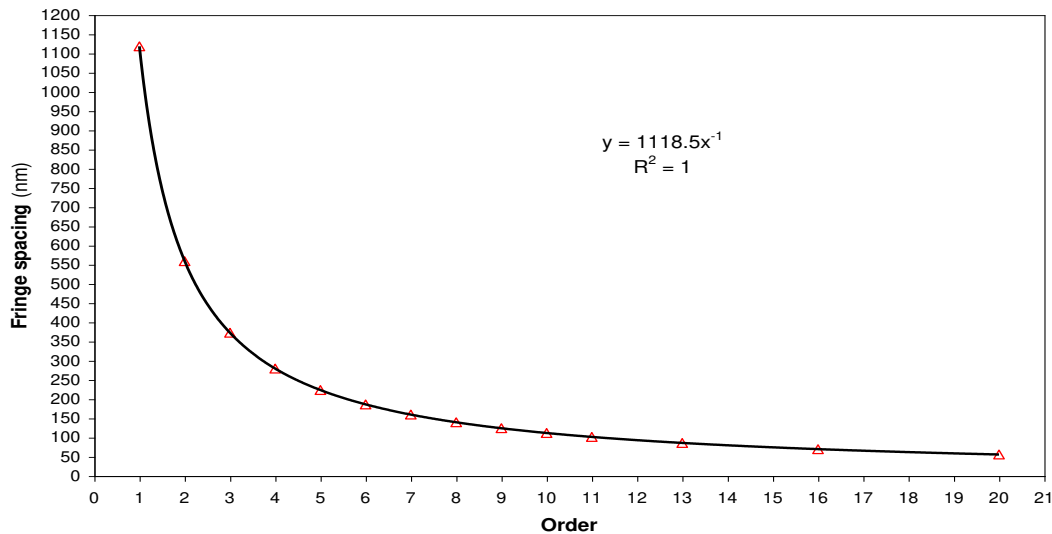
Figure 7. Third family of fringes present in the FT of the diffraction pattern of the microsphere captured by the CCD camera.

Each beam produces its own diffraction order and in Figure 8 the angles of each zero order beam are called θ_{s0} and θ_{p0}, while the angles corresponding to the first orders are called θ_{p1} and θ_{s1}, respectively. The symmetrical orders corresponding to the diffractions ±1 are not indicated. Upon arrival to the interface between the microscope slide and the saline solution all the orders experience total reflection and produce electromagnetic evanescent fields that, interacting with the solution, produce, through scattering, propagating beams. Due to the preservation of the momentum, the resultant vectors corresponding to the different evanescent waves continue with their trajectory in the saline solution and are indicated with the symbol $\vec{k}$ with the subscripts corresponding to the different wave fronts. There is one important point to remark here: no fringes exist before the evanescent field is converted into propagating waves at the level of the interface between the microscope slide and the saline solution. The values of the pitches measured through the process of taking a FFT of the image captured by the microscope correspond to the scattered light beams produced in the saline solution. Specifically, they correspond to the gradients of the retardation of the fringe families in the direction of the coordinate axis X, as it is shown in Figure 2a. These fringes are observed at the FT plane of the spherical relay lens (i.e. the polystyrene microsphere) and the numerical FT provides the pitches of the fringes which are themselves equivalent to diffraction gratings of equation $(\sin\theta_i + \sin\theta_n) = np$, where θ_i is the angle of incidence of the il-

luminating beam and θ_n is the angle that the diffraction order n makes with the direction of the illumination beam. The grating equation is in agreement with the generalization made by Toraldo Di Francia which has been formalized by Eq. (7).
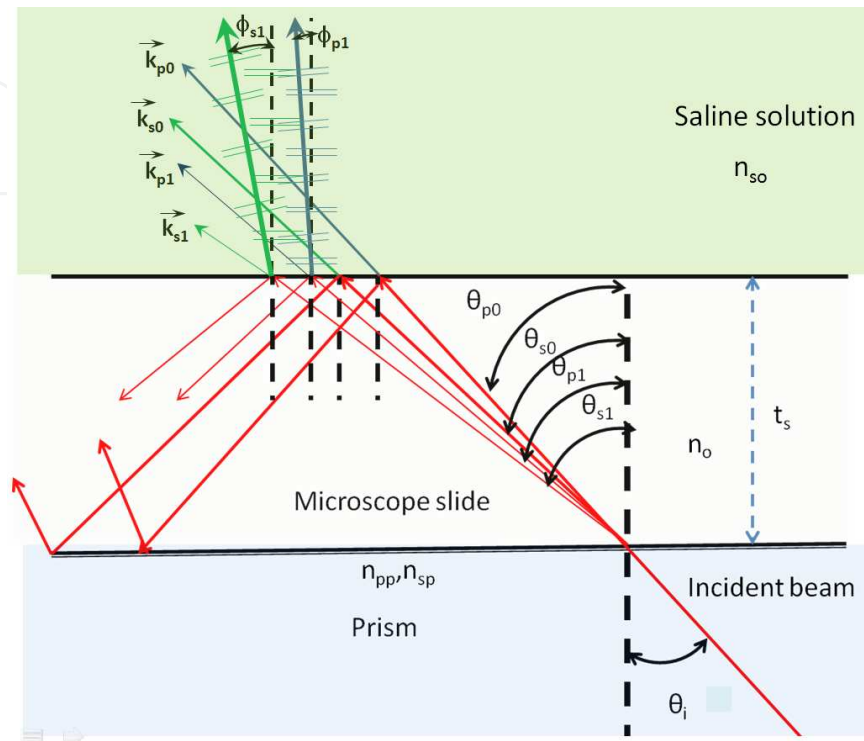

Figure 8. Beams forming the system of rectilinear fringes observed with the optical microscope

Unlike an ordinary diffraction grating, the residual stresses from one incident beam produce two sets of diffraction orders, one corresponding to the ordinary beam and another corresponding to the extraordinary beam. Furthermore, these two beams are orthogonally polarized. The law of refraction at a boundary with a uniaxial birefringent material can be written (see Figure 9):

$$
\begin{cases}
\vec{k}_i \sin\theta_i = \vec{k}_o \sin\theta_{p0} \\
\vec{k}_i \sin\theta_i = \vec{k}_o \sin\theta_{s0}
\end{cases}
\tag{13}
$$

While the first equation of Eqs. (13) corresponds to the classical Snell's law, the second relationship does not because the extraordinary beam does not obey this law. As illustrated in the insert of Figure 9, the wave front of the extraordinary beam is not normal to the ray. In the case of the uniaxial crystal, the ordinary and extraordinary beams are parallel to each other and the ray velocity of the extraordinary beam is different from the wave front velocity.
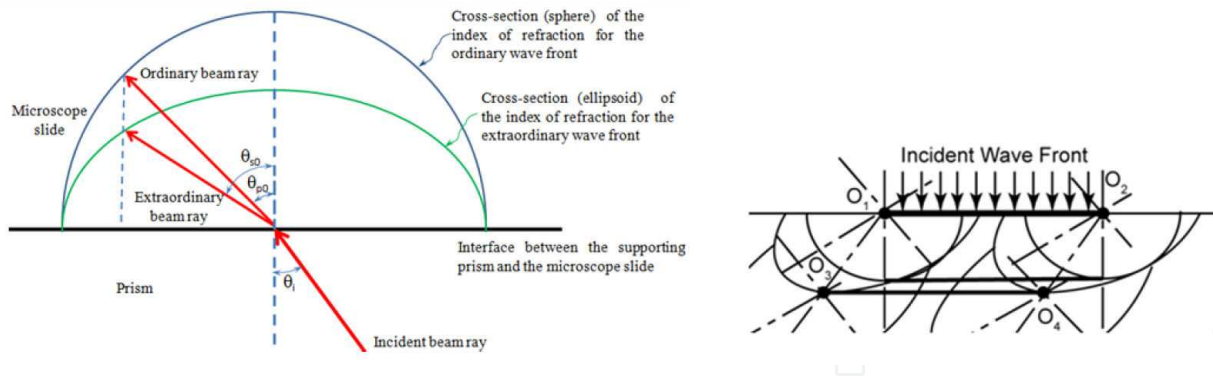
Figure 9. Interface of the prism with the slide rays corresponding to the ordinary and extraordinary beams. The insert in the right side of the figure shows that in the case of an uniaxial crystal the ordinary and extraordinary wave fronts are parallel.

All the diffraction beams that are produced in the interface prism-microscope slide have separate trajectories in the microscopic slide and upon arriving at the interface of the saline solution-microscope slide are totally reflected and produce evanescent wavefronts that generate the families of observed fringes. In view of the conservation of momentum of the photons, the resulting vectors $\vec{k}_{p0}$, $\vec{k}_{s0}$, $\vec{k}_{p1}$ and $\vec{k}_{s1}$ continue their trajectories in the saline solution. The vectors $\vec{k}_{p0}$ and $\vec{k}_{s0}$ are the limit beams that experience total reflection. The vector $\vec{k}_{p1}$ has components,

$$k_{p1x} = \frac{2\pi}{\lambda_e} n_0 \sin\theta_{p1} \tag{14}$$

$$k_{p1z} = \frac{2\pi}{\lambda_e} i \sqrt{n_0^2 \sin^2\theta_{p1} - n_{so}^2} \tag{15}$$

where λ_e is given by equation (10). The modulus of the k-vector is

$$\left\| \vec{k}_{p1} \right\| = \frac{2\pi}{\lambda_e} \sqrt{2n_0^2 \sin^2\theta_{1p} - n_{so}^2} \tag{16}$$

It is possible to see that as the orders increase, the k-vector component k_{pnz} in the Z-direction decreases while the k-vector component k_{pnx} in the X-direction increases, and the two components are super-oscillatory. The diffraction orders that are observed in the FT of Figure 5d were indicated in Figure 8 by the angles ϕ_{p1} and ϕ_{s1} that they make with the direction of observation, Z-direction. The corresponding sines of the above mentioned angles are:

$$\begin{cases} \sin\phi_{pm} = \dfrac{\lambda}{n_{so}\, p_{pm}} \\[3mm] \sin\phi_{sm} = \dfrac{\lambda}{n_{so}\, p_{sm}} \end{cases} \tag{17}$$

where p_{pm} and p_{sm} are extracted from Figure 5d in correspondence of the order m currently being considered. The experimental values hence are:

$$\begin{cases} \sin\phi_{pm} = \dfrac{0.6328}{1.36 x 3.356} = 0.13683 \\[3mm] \sin\phi_{sm} = \dfrac{0.6328}{1.36 x 2.238} = 0.20791 \end{cases} \Rightarrow \begin{cases} |\,\phi_{pm}\,| = arc\,\sin(0.136834) = 7.9693^o \\[2mm] |\,\phi_{sm}\,| = arc\,\sin(0.20791) = 12.0^\circ \end{cases}$$

The above angles define two families of scattered light photoelastic fringes that give the gradients of the absolute retardation of the beams traveling parallel to the surface of the prism. The upper face of the prism has a state of residual stresses generated during the fabrication of the glass slab where the glass of the prism was extracted. Residual stresses are created in the process of cooling of the slab. These residual stresses are compressive in the faces of the slab and tensile inside the slab. The compressive stresses are located in a small region across the total height of the slab. Because the field observed by the microscope is very small and the stresses are uniform in this field, the gradient is lineal and the observed fringes must have a uniform pitch. The pitches that have been observed can be related to the gradient of the uniform stresses of the outer layer of the prism. These gradients can be expressed as follows:

$$\frac{d\delta_{px}}{dx} = n_{pp} - n_o = A\sigma_1 + B\sigma_2 \tag{18}$$

$$\frac{d\delta_{sx}}{dx} = n_{sp} - n_o = B\sigma_1 + A\sigma_2 \tag{19}$$

The second terms of the equations (18,19) are the Maxwell-Neumann equations that relate the absolute retardations to the principal stresses σ_1 and σ_2. In the current case, since residual stresses are both compressive, it holds $\|\sigma_1\| < \|\sigma_2\|$.

By subtracting Eq. (19) from Eq. (18), one gets:

$$\frac{d\delta_{px}}{dx} - \frac{d\delta_{sx}}{dx} = \frac{d\delta_3}{dx} = (A - B)(\sigma_1 - \sigma_2) = C(\sigma_1 - \sigma_2) \tag{20}$$

This last equation corresponds to the family of fringes plotted in Figure 7. Approximate solutions for these equations were presented in references [9,10]. A new set of values are given in Table 2. The index of refraction of the microscope slide was corrected to 1.51509 from the

value of 1.5234 originally indicated by the manufacturer. This was done because the experimental measurements required the use of red light (i.e. $\lambda=0.6328$ µm). The indices of refraction n_{pp} and n_{ps} of the ordinary and extraordinary beams travelling in the optical system were determined by combining equations (18-20) and optimization techniques. The photoelastic constants of glass were taken from values obtained for optical glass by H. Favre, Polytechnic Institute of Zurich, Switzerland.

p_{pm}	3.356±0.060 (µm)	n_{pp}	1.52082	n_{so}	1.36	A	$-0.565 \cdot 10^{-11} m^2/N$	σ_1	-147 MPa
p_{sm}	2.238±0.0019 (µm)	n_{sp}	1.52061			B	$-3.160 \cdot 10^{-11} m^2/N$	σ_2	-155 MPa
p_{ps}	1.118±0.0025 (µm)	n_o	1.51509			C	$2.571 \cdot 10^{-11} m^2/N$	$\sigma_1 - \sigma_2$	8 MPa

Table 2. Determination of residual stresses and indices of refraction from measured values of diffraction angles and retardations.

The obtained results support the assumptions concerning the presence of systems of lines in the captured images and their source in the residual stresses present on the glass of the prism.

5. Diffraction patterns of the observed objects

In Figure 2a, it was illustrated one of the geometrical configurations observed in this research wok (i.e. a prismatic object), the type of field originated by the evanescent illumination and, from the literature, it was described the near field configuration in the neighbourhood of a prismatic nano-crystal. In the obtained images there are diffraction patterns produced by the presence of NaCl nano-crystals on the microscope slide. However, these diffraction patterns are not classical patterns of diffraction produced by illuminating the object with wave fronts originated at a source and diffracted by the object. In this case, the object interacts with an electromagnetic field (i.e. the evanescent field) and such interaction causes the object to emit light. This light propagates through diverse media and arrives to a sensor that captures the image. The image captured is the diffraction pattern of the object. Figure 10 shows the light path from the source to the sensor.

From the preceding developments, the scattered light is produced at the interface between the microscope slide and the saline solution. Figure 2 shows right the main beam arriving to the interface, the vector $\vec{k}$ and its components k_x and k_z. From the preceding section, we know that there are many other evanescent plane wave fronts that also impinge in the observed object and hence will produce scattered patterns that will be present in the formed image of the object in a similar way to the description provided for the effect of the beams in the saline solution but will experience different path changes because the index of refraction of the sodium-chloride nano-crystals is higher than the index of refraction of the saline solution. The observed diffraction patterns in the collected images have a structure shown in Part 4 of Figure 10. The images show a diffraction pattern that outlines the object contour in a similar way to the outline depicted in Figure 2by the near field (this pattern can be as-

sumed to be a zero order of diffraction), and two shifted images that can be assumed to be diffraction orders ±1. These images are generated in the object itself (nano-crystal) that emits light through the scattering process since no light passes from the microscope slide to the crystal but there is only an evanescent electromagnetic field penetrating in the nano-crystal. It is possible to understand then that the observed pattern is not a classical diffraction pattern and hence what we observe is not the classical FT of the object as it occurs in the case of an illuminated object.
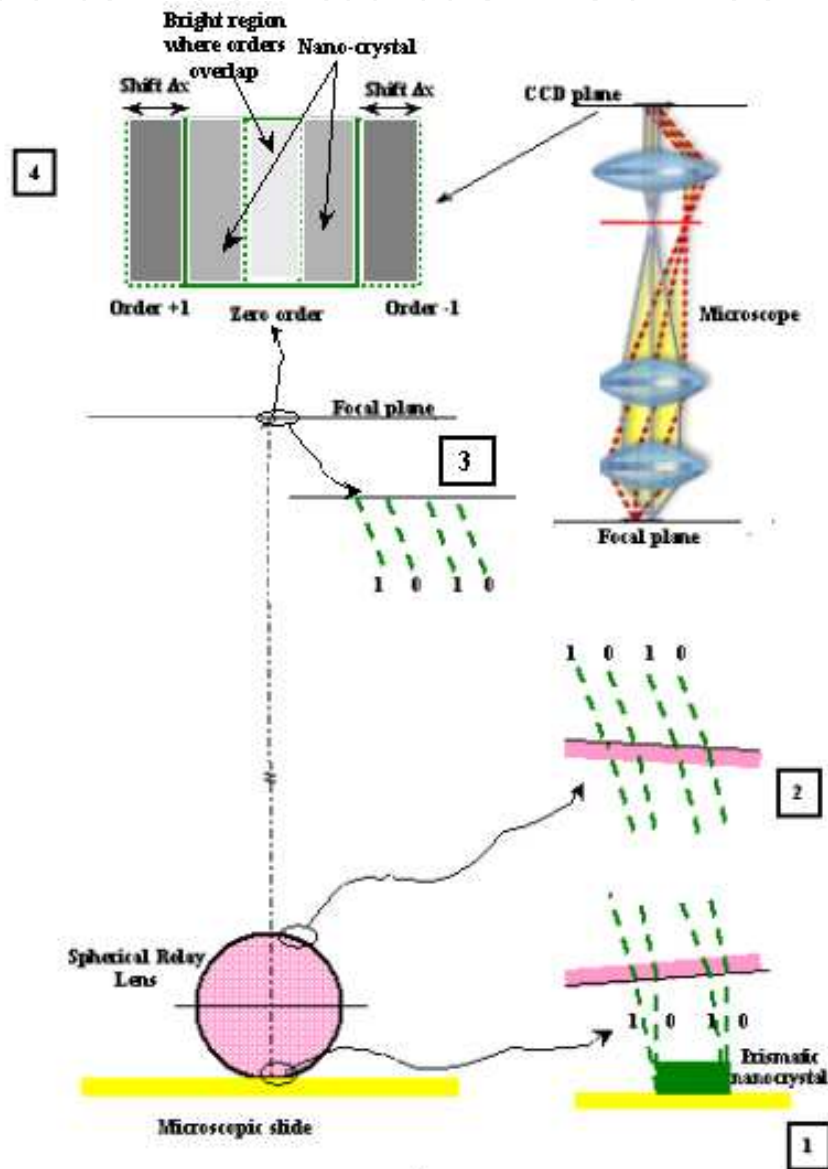
Figure 10. Schematic representation of the optical system leading to the formation of lens hologram: 1) Prismatic nano-crystal; 2) Wave fronts entering and emerging from the polystyrene microsphere acting as a relay lens; 3) Wave fronts arriving at the focal plane of the spherical relay lens; 4) Wave fronts arriving at the image plane of the CCD. The simulation of the overlapping of orders 0, +1 and -1 in the image plane of the CCD is also shown.

The same point brought in the case of the observed scattered light photoelastic fringes applies to the crystals. The fringes are present in the interface microscope slide-saline solution and are captured by the microscope through the small sphere acting as a relay lens. To get the diffraction pattern of the fringes required a numerical FT of the image (Figure 5d). The same concept applies to the diffraction pattern of the nano-crystals, to get their diffraction patterns it is necessary to perform a numerical FT. Hence, the observed images have a direct connection with the geometry of the object as shown in Figure 2, but the traditional relationships between the object and the optical FT of the object do not apply.

In [19], the conversion of the evanescent field into scattered light waves is explained in terms of Brillouin-Raleigh scattering. The evanescent field through resonance causes the crystals to vibrate in their eigenmodes. These vibrations cause phonon-photon interactions that produce the light emission. The eigenmodes depend on the crystal sizes and hence the different crystals emit light of different frequencies. There is a correlation between light color and crystal size and the emitted frequencies are present in the reflectance energy spectrum of NaCl [19]. The color camera images provided approximate image frequencies through a graphical plot of frequency vs. color for the camera sensor.

All the observed objects are localized in a region that is very close to the vertical axis of the relay lens in a radius smaller than one micron. Hence, the boundary conditions of the problem concerning the diffraction patterns of the observed prisms and nano spheres are very complex. An analysis of the electrical field amplitude [2,16] shows that the energy of the field is concentrated in a very small region (see Figure 11).
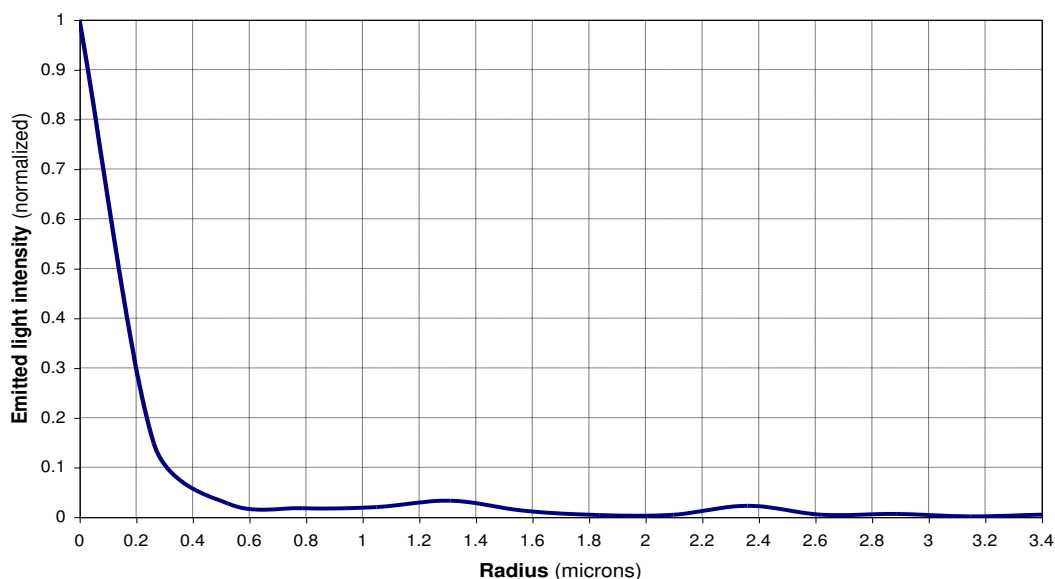

Figure 11. Intensity light distribution at the contact plane between the polystyrene microsphere and the supporting microscope slide

As is shown in Figure 2, the intensity of the field in the neighborhood of the particle is very complex but tends to resemble the object itself. In the present case, there is a resonance phe-

nomenon that causes the emission of wave fronts that are captured by the microscope camera sensor.

6. Propagation of the wave fronts emerging from the observed object to the camera sensor

The diffraction wave fronts generated by the observed objects reach the sensor by propagating through the relay lens that concentrates the beams in its focal region, then through the saline solution, air, and finally through the microscope optical path to arrive to the sensor. Since the propagating wave fronts are beyond the resolution limit, this fact implies that we are dealing with the propagation of solitons.

Following the arguments presented in reference [20] and referring to the coordinate system shown in Figure 2a, a wave front propagating in the Z-direction can be represented as:

$$\vec{E}(x,y,z,t) = E_o(x,y)e^{i(\vec{k}z-\omega t)} \tag{21}$$

where $E_o(x,y)$ is the transversal amplitude profile of the wave front. If the temporal component is removed the amplitude reduces to:

$$\vec{E}_s(x,y,z) = E_o(x,y)e^{i(\vec{k}z)} \tag{22}$$

The spatial component must satisfy the stationary Helmholtz equation:

$$(\nabla^2 + \vec{k}^2)\left\{\vec{E}_s\right\} = 0 \tag{23}$$

Since the amplitude $E_o(x,y)$ is independent of Z, the intensity $\vec{E}_s\vec{E}_s^* = I$ of the propagating wave is constant. Utilizing the method of variables separation, the solution of the partial differential equation (23) can be separated into the transversal component and in the longitudinal component. By expressing this solution in cylindrical coordinates one gets:

$$\vec{E}_{sc}(r,\theta,z) = \vec{E}_{sr}(r)\vec{E}_{s\theta}(\theta)e^{i(\vec{k}z)} \tag{24}$$

The $\vec{E}_{s\theta}(\theta)$ is a periodic function of θ of the form $\vec{E}_{s\theta}(\theta) = E_{s\theta}e^{im\theta}$ (m=0,1,2,…). By replacing this solution in (24) and introducing Eq. (24) in the Helmoltz's equation (23), it is obtained a

partial differential equation of the second order in r whose solution is formed by a combination of Bessel function of the first kind and Neumann functions.

From the above outlined mathematical model a number of different kinds of propagating beams can be derived. In the present case discussed in this chapter, the propagating waves correspond to super-resolution electromagnetic fields. The particular problem that we are considering is extremely complex. It can be shown that this type of solitons require polarization in the direction of propagation. Hence, the solution of the problem requires functions that provide longitudinal polarization propagating in free space with super-resolution and uniform amplitude along the direction of propagation. A partial answer to this problem can be found in [21,22] where it is shown that such a type of wave fronts can be obtained by phase modulation and beam focusing by a high aperture focusing lens. In the particular problem dealt with in this chapter the relay lens has this property and it will generate this type of wave front in the focal plane. The experimental results obtained in the present study seem to support this model for the propagation of the diffraction patterns of the observed objects to the microscope camera sensor. For example, Figure 11 shows that the intensity pattern $I = \vec{E}_{sr}^2 + \vec{E}_{s\theta}^2$ at the interface between the microscope slide and the polystyrene microsphere that acts as relay lens presents a very strong axial field.

7. Observation of prismatic nano-objects

The process of observation of the objects present in the central spot of the image shown in Figure 5c was the following. First, the objects are located by observing the image. The portion of the image that includes the object to be analyzed is then extracted. The cropped image is magnified and then repixelated via bicubic spline either to 512x512 or 1024x1024 increasing thus numerically the resolution.

Figures 12 and 13 show two examples of the captured nano-crystals images, the isophote lines (lines of equal intensity) and the FT of the images. The isophote lines are similar to the field intensity lines shown in Figure 2. In Figures 12a and 12b, there are respectively shown the monochromatic image and the color image of a particle with a square cross-section in the plane of the image. A detailed analysis of the particle of Figure 12 a will be presented later in the chapter. Figure 13e includes the theoretical isomeric structure of the NaCl nano-crystal [23] corresponding to the structure observed experimentally.

The dimensions of the crystals can be obtained by utilizing a Sobel filter to detect the edges in the corresponding images as shown in Figure 14. In these figures, the zero and the first orders are outlined following the schematic representation of Part 4 of Figure 10. One nano-crystal has a square cross-section of side length 86 nm. The dimensions of the other nano-crystal in the plane of the image are 120x46 nm.
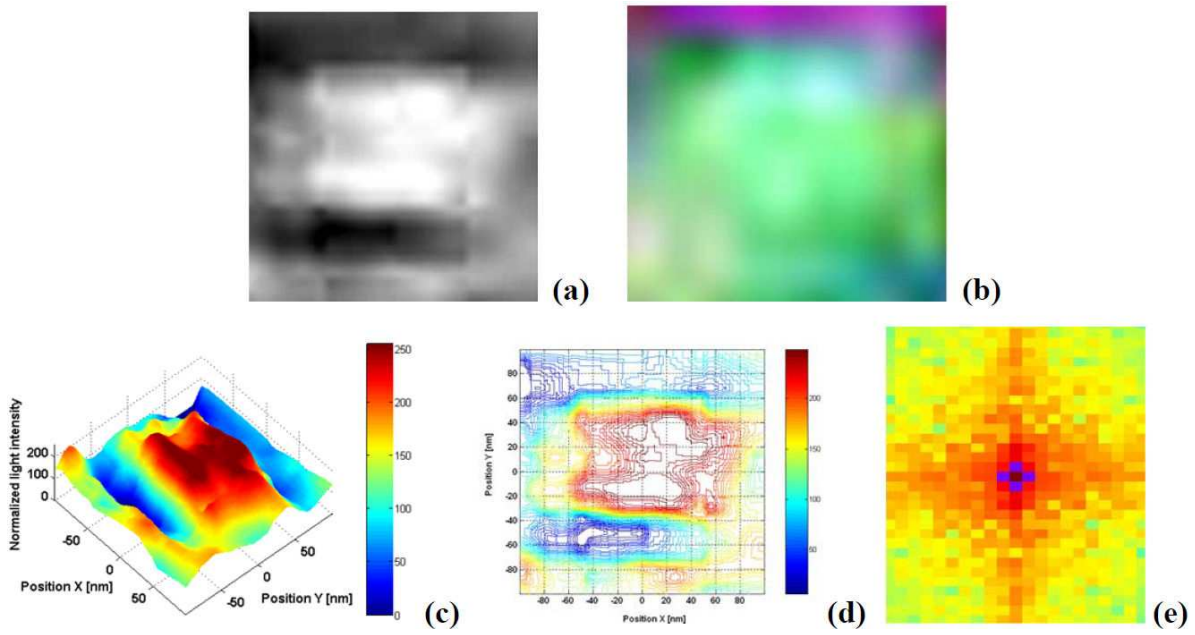
Figure 12. NaCl nano-crystal of length 86 nm: (a) gray-level image (1024 x 1024 pixels); (b) Image of the nano-crystal captured by a colour camera; (c) 3-D distribution of light intensity; (d) Isophote lines; (e) FT pattern of the image of the nano-crystal recorded by the sensor.
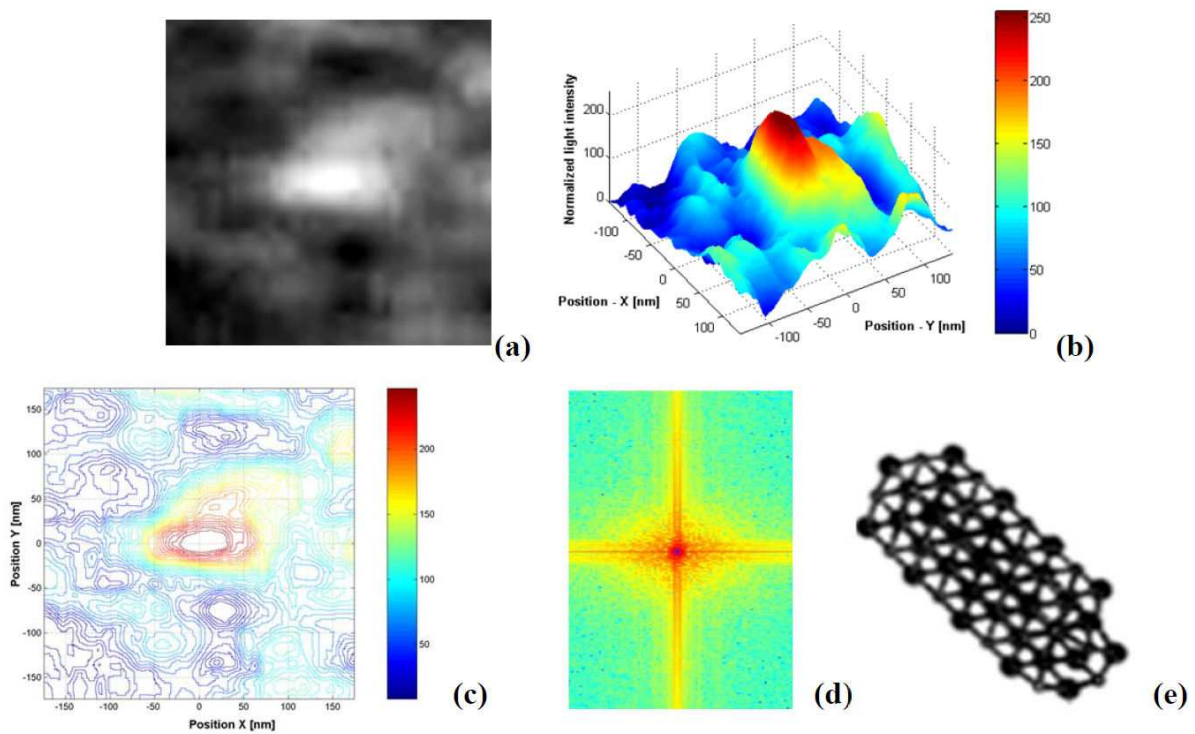

Figure 13. NaCl nano-crystal of length 120 nm: (a) Gray-level image properly repixelated; (b) 3-D distribution of light intensity; (c) Isophote lines; (d) FT pattern of the image of the nano-crystal recorded by the sensor; (e) Theoretical crystal structure [23].
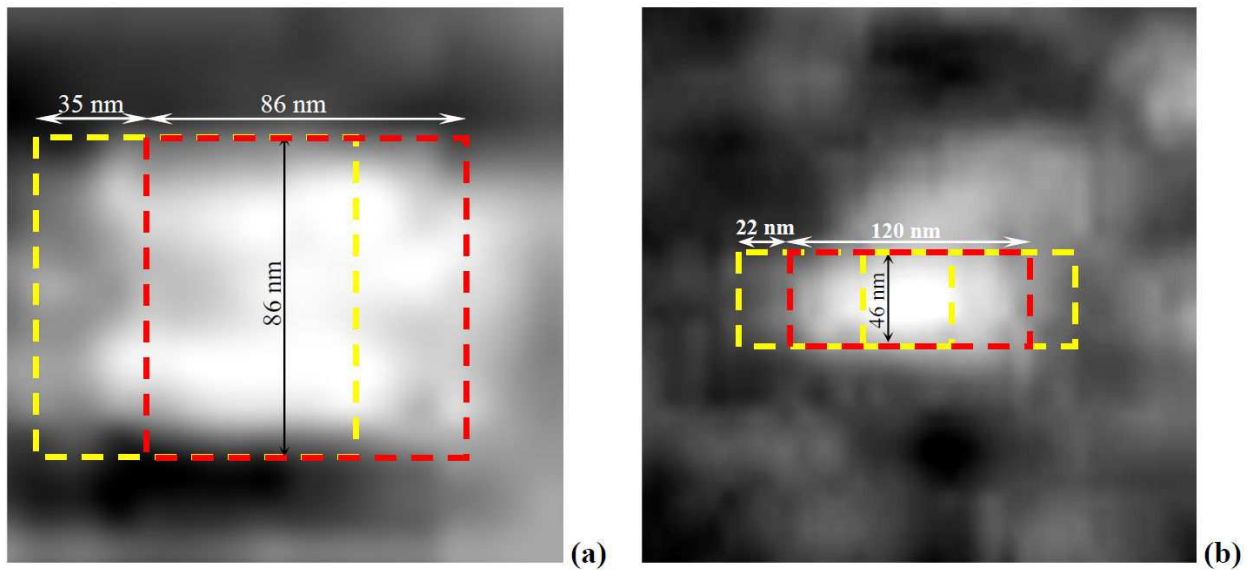
Figure 14. Edge detection process for determining main geometric dimensions of NaCl nano-crystals: a) L=86 nm; b) L=120 nm.
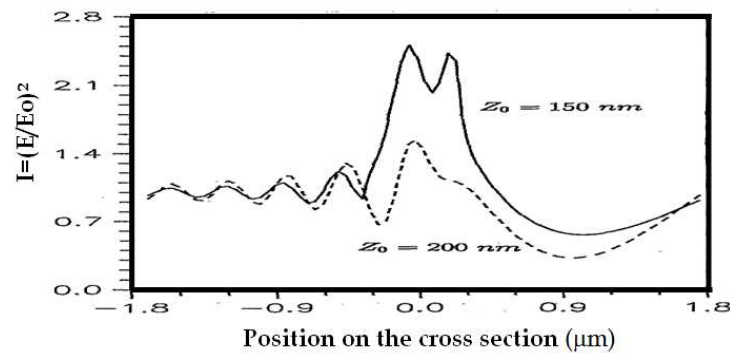

Figure 15. Cross-section of the electromagnetic field intensity in the neighborhood of a particle of prismatic shape as those indicated in Figure 2b. z_o gives the level of the cross-section with respect to the plane supporting a particle of 150 nm depth.

Figure 15, taken from reference [4], shows the intensity of the electromagnetic field in the neighborhood of a prismatic particle illuminated by an evanescent field. As it can be seen, the intensity gradient is sharp at the edges of the prism and, hence, the edge detection filter is a useful tool to locate the prism edges.

8. Recovery of the depth information

As mentioned previously, the photoelastic gradient fringes produced by the different diffractions orders at the interface of the prism-microscope slide experience phase changes that provide depth information. These fringes are carrier fringes that can be utilized to extract

optical path changes. This type of setup to observe phase objects has been used in phase hologram interferometry as a variant of the original set ups proposed by Burch et al. [24] and Spencer and Anthony [25]. When the index of refraction in the medium is constant, the rays going through the object are straight lines. If a prismatic object is illuminated with a beam normal to its surface, the optical path s_{op} through the object can be determined by computing the integral:

$$s_{op}(x,y) = \int n_i(x,y,z)dz \tag{25}$$

where the direction of propagation of the illuminating beam is the Z-coordinate and the analyzed plane wave front is the plane X-Y; $n_i(x,y,z)$ is the index of refraction of the medium.

The change experienced by the optical path is given by:

$$\delta_{op}(x,y) = \int_0^t \left[n_i(x,y,z) - n_o \right] dz \tag{26}$$

where t is the thickness of the medium. Assuming that:

$$n_i(x,y,z) = n_c \tag{27}$$

where n_c is the index of refraction of the observed nano-crystals. By replacing Eq. (27) in Eq. (26), the latter becomes:

$$\delta_{op}(x,y) = \int_0^t \left[n_i(x,y,z) - n_o \right] dz = (n_c - n_o)t \tag{28}$$

By transforming Eq. (28) into phase differences and making $n_o = n_{so}$, where n_{so} is the index of refraction of the saline solution containing the nano-crystals, one can write:

$$\Delta\phi = \frac{2\pi}{p_{fr}}(n_c - n_{so})t \tag{29}$$

where p_{fr} is the pitch of the fringes generated as the light goes through the specimen thickness. In general, the change of path is small and no fringes are observed. In order to solve this problem carrier fringes can be added. An alternative procedure is the introduction of a grating in the illumination path [26]. In the case of the nano-crystals, the carrier fringes can be obtained from the FT of the lens hologram of the analyzed crystals. Details of the procedure to carry out this task are given in [19].

9. Example of the digital reconstruction of a nano-crystal

Having obtained the shape of the section of the prism and the depth it is possible to reconstruct a crystal. The results of this process are summarized in Figure 16. The 5x4x4 nano-isomer of NaCl (Figure 16b) is interesting because has one step in the upper part of the crystal [23]. This step is correctly recovered in the numerical reconstruction. Figure 16a shows the numerical reconstruction of this crystal, consistent with the theoretical structure; Figure 16c shows the level lines of the top face; Figure 16d shows a cross-section where each horizontal line corresponds to five elementary cells of NaCl. Since the upper face of the nano-crystal is not very likely to be exactly parallel to the camera plane, there is an inclination which can be corrected by means of an infinitesimal rotation. By performing this operation, the actual thickness jump in the upper face of the crystal (see the theoretical structure in Figure 16b) is obtained. The jump in thickness is 26 nm out of a side length of 86 nm: this corresponds to a ratio of 0.313 which is very close to theory. In fact, the theoretical structure predicts a vertical jump of one atomic distance vs. three atomic distances in the transverse direction: that is, a ratio of 0.333.
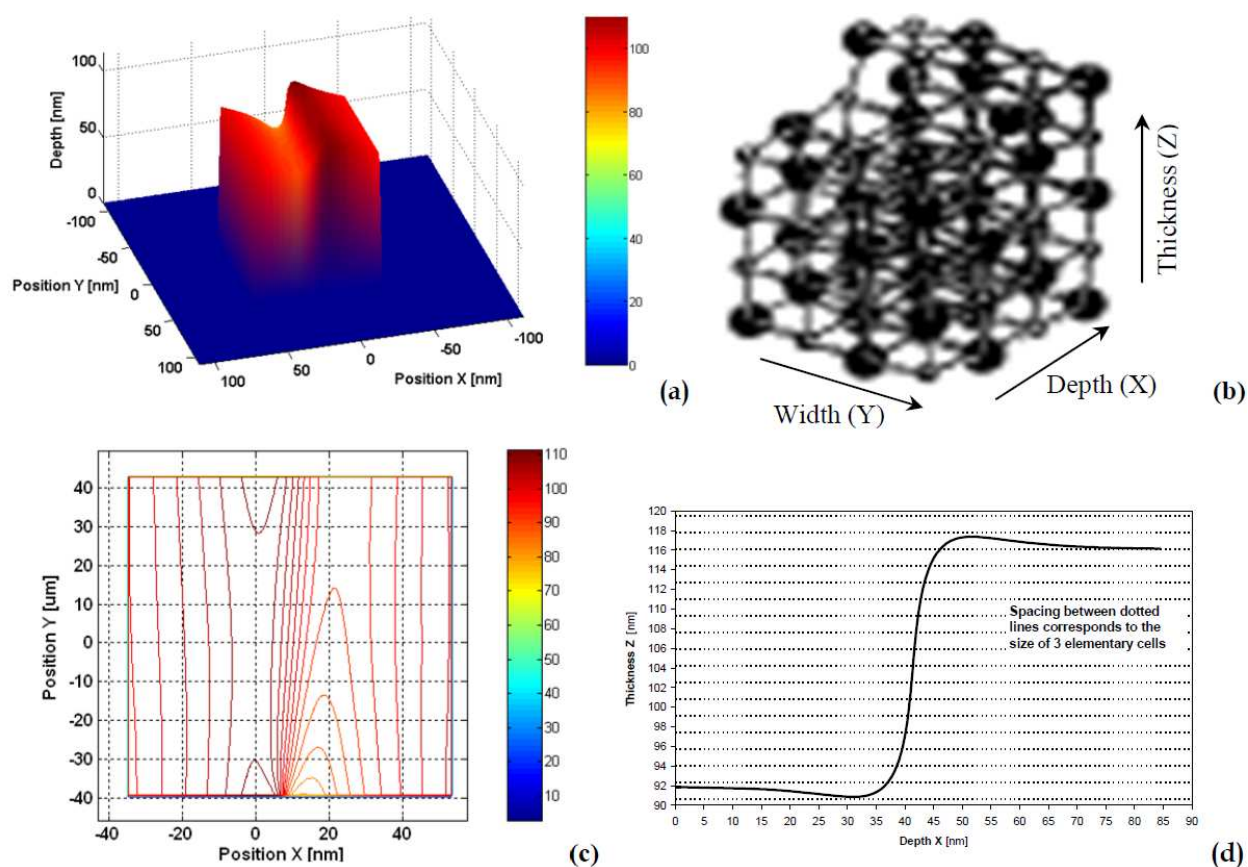

Figure 16. (a) Numerical reconstruction of the NaCl nano-crystal of length 86 nm, the crystal is inclined with respect to the image plane; (b) 5x4x4 theoretical structure of the nano-crystal; (c) Level lines; (d) Rotated cross-section of the upper face of the nano-crystal: the spacing between dotted lines corresponds to size of three elementary cells.

10. Verification of some of the assumptions of the developed model to observe nano-size objects

A further analysis of the image of the 86 nm prismatic nano-crystal provides more insight on the process of formation of the recorded images. In Figure 12a, it is possible to see the image of the particle and the presence of background fringes that go across the image. A partial simulation of the image in the X-direction was carried out by adding to a uniform illumination zero order two shifted orders in the X- and in the Y-directions and adding the image of a sinusoidal background fringe. The results of the simulation are presented in Figure 17. The simulated image (Figure 17a) is very similar to the image of the nano-crystal recorded by the CCD camera (Figure 17b).

Figure 18 is obtained by considering only the zero order of the FT pattern of the nano-crystal. By adopting a 4x4 low-pass filter centered in (0,0) one obtains the filtered image shown in Figure 18a. By masking the image with a mask corresponding to the position of the nano-crystal in the recorded image, Figure 18b is obtained. The isophote lines for the filtered-unmasked zero order image and for the filtered-masked image are shown in Figures 18c and 18d, respectively. It can be seen that there is a strong resemblance between the two images indicating the plausibility of the adopted interpretation supported by the developed models of the image formation process. The masked zero order has an almost uniform intensity distribution that is not completely uniform because the crystal is not symmetric in the X-direction but the intensity distribution is almost uniform as it was assumed in Part 4 of Figure 10.
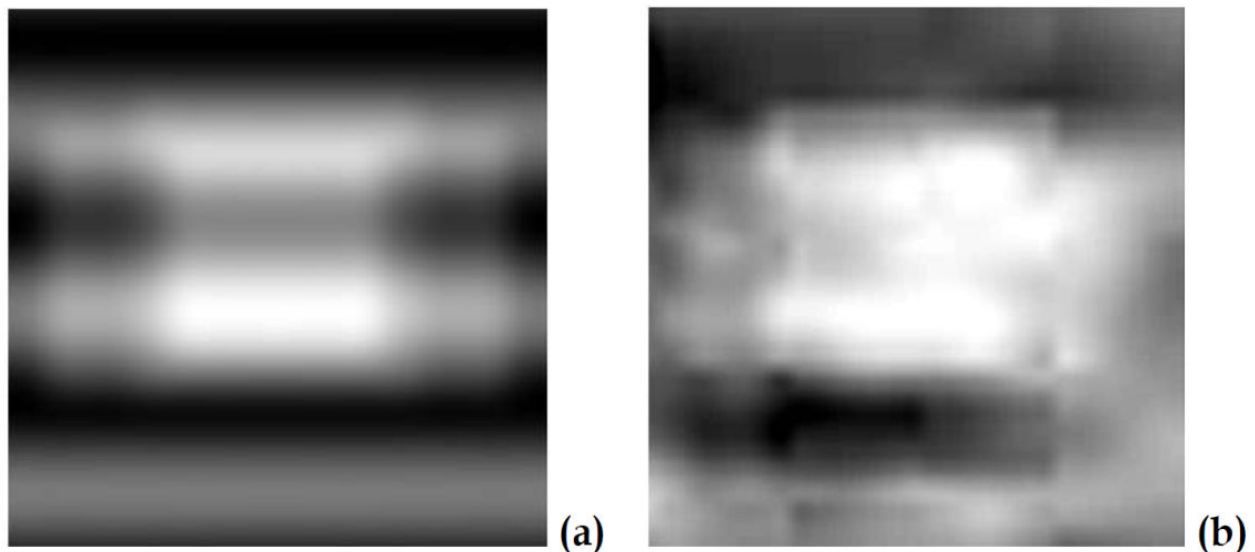

Figure 17. (a). Simulated image of the 86 nm nano-crystal obtained by adding up the zero order, two shifted orders in the X-direction and a sinusoidal background fringe pattern; (b) Actual image of the nano-crystal recorded by the CCD camera.
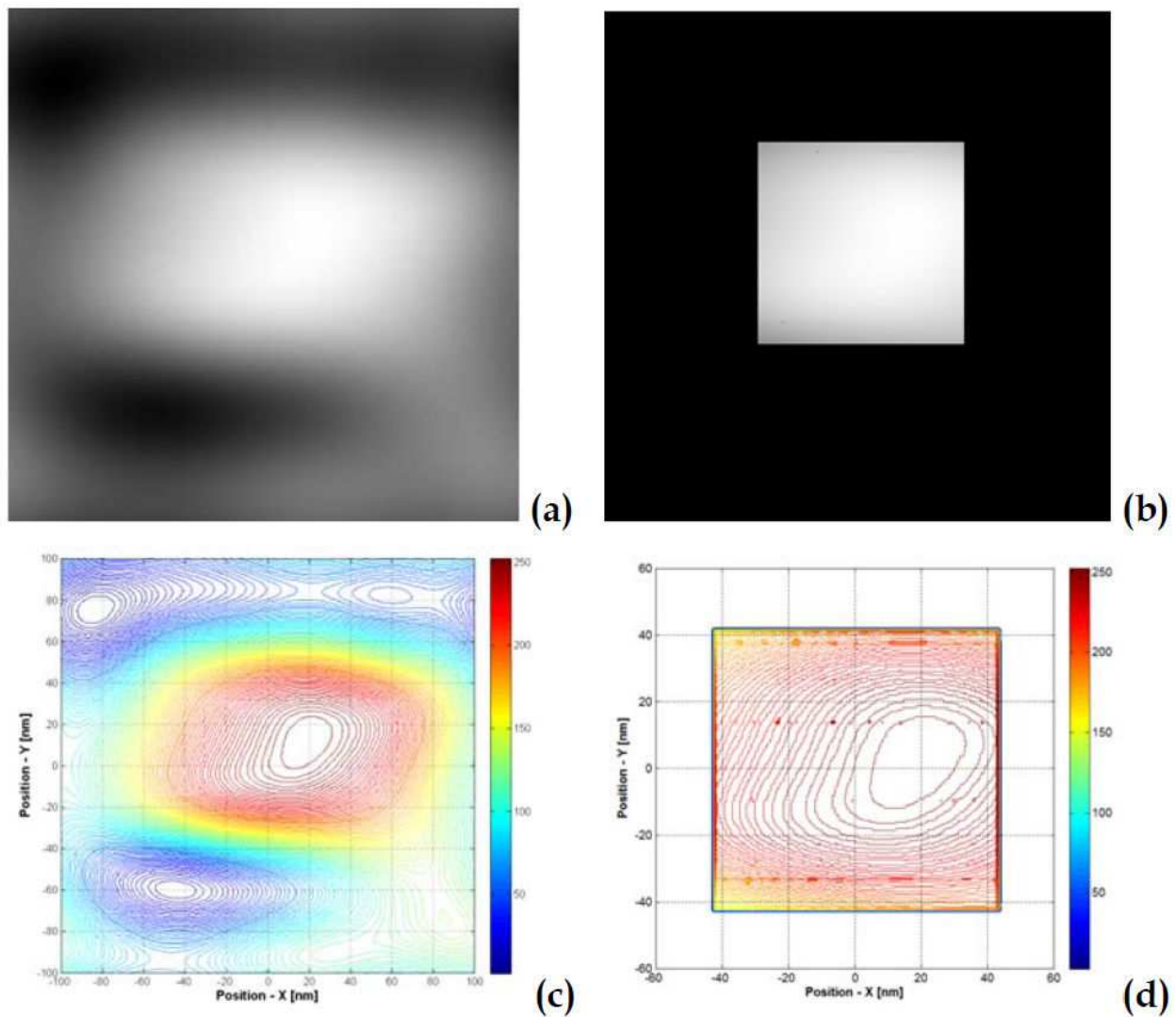
Figure 18. (a) Filtered zero order of the 86nm nano-crystal image (Figure 12a) obtained by using a 4x4 low-pass filter; (b) Masking of the filtered zero-order of Figure 18a with a mask corresponding to the region occupied by the nano-crystal; (c) Isophote lines of the filtered image shown in Figure 18a; (d) Isophote lines of the masked filtered image shown in Figure 18b.

The recorded images are originated in scattered wave fronts that, as shown in Figure 4b, are observed in the Z-direction but provide information of events that occur in the X-Y plane. Hence, in order to analyze the information coming from the X-Y plane, one needs to deal with the real part of the FT pattern shown in Figure 12e (i.e. that relative to the 86 nm nano-crystal). The FT of the real part of the FT of Figure 12e was computed. Figure 19a shows the FT of the real part of the FT of Figure 12e. The pattern presents different diffraction orders with a complex structure. These orders contain information concerning features of the re-corded image of the nano-crystal. This information can be retrieved by filtering the orders and getting the inverse FT. Figure 19b is the result of filtering the zero order of Figure 19a and taking the inverse FT. This figure provides information concerning the sources that con-tribute to form the zero order of the image.

Figure 19b includes seven peaks representing the FT of the wave fronts that form part of the image of the diffraction pattern of the nano-crystal. The two peaks recorded farther apart in the Y-direction correspond to the fringes that are in the background of the image and represent the system of fringes discussed in the section "*Generation of multiple k-vectors*". These fringes are independent of the formation of the image of the diffraction pattern of the observed nano-crystal.

The other five peaks included in Figure 19b correspond to the FT of the observed diffraction orders, the zero order and the orders ±1 in the X- and in the Y-directions. The filtering of the two diffraction orders ±1 indicated in Figure 19a provides the components that form the structure of the orders ±1. These components are shown in Figure 19c and Figure 19d for the X-direction (i.e. the harmonics are selected in the f_x-direction) and in the Y-direction (i.e. the harmonics are selected in the f_y-direction), respectively.
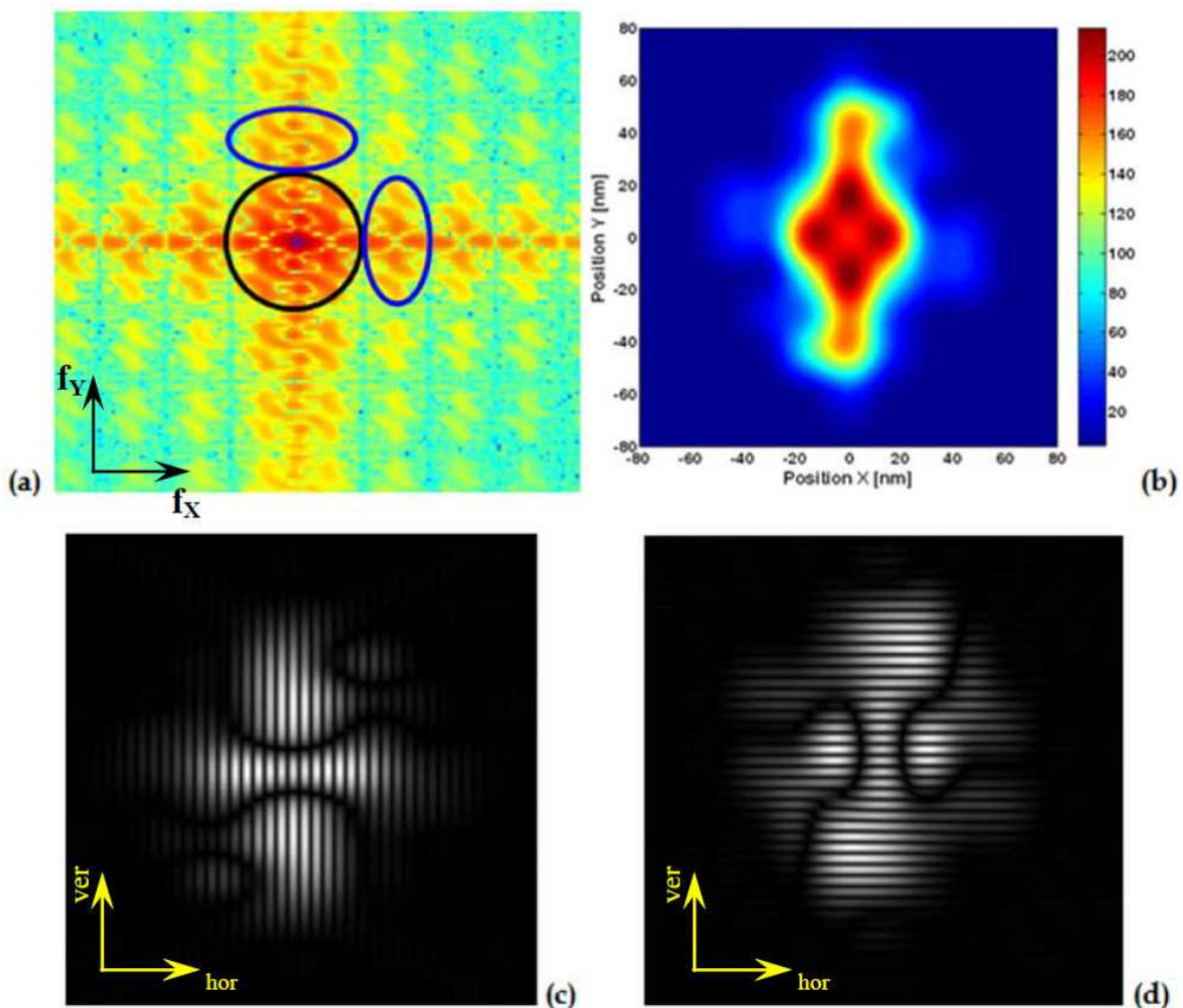

Figure 19. (a) FT of the real part of the FT of the 86 nm prismatic nano-crystal and filtered components; (b) 2-D view of the filtered zero order extracted from the real part of the FT pattern of the nano-crystal; (c) Result of filtering first order in the f_x-direction of the FT pattern shown in Figure 19a; (d) Result of filtering first order in the f_y-direction of the FT pattern shown in Figure 19a.

The cross-sections of the filtered components shown in Figures 19c-d are plotted in Figure 20a-d. Figure 20a corresponds to the cross-section in the horizontal direction (i.e. "hor" in Figure 19c) of the pattern obtained by filtering the f_x–orders ±1. Figure 20b corresponds to the cross-section taken in the vertical direction (i.e. "ver" in Figure 19c). While the filtered pattern is modulated in amplitude along the horizontal direction (see Figure 20a), we see in the vertical direction a central peak at Y=0 and two lateral peaks located at Y=17.6 nm from this central peak (see Figure 20b).

Figure 20c corresponds to the cross-section in the horizontal direction (i.e. "hor" in Figure 19d) of the pattern obtained by filtering f_y–orders ±1. Figure 20d corresponds to the cross-section in the vertical direction (i.e. "ver" in Figure 19d). While the filtered pattern is now modulated in amplitude along the vertical direction (see Figure 20d), we see in the horizontal direction a central peak in X=0 and two lateral peaks located at X=13.8 nm from this central peak (see Figure 20c). Since the crystal is not symmetric in X- and Y-directions, one should expect some difference between the two resonant frequencies.

The distance between the central peak and the lateral peaks in the cross-section represented in Figure 20c coincides with the spatial frequency of the vibration nodes of the nano-crystal in the X-direction resulting from the model introduced in Ref. [19] and that at the same time is a multiple of the elementary cell of the NaCl, 24 d, where d=0.573 nm is the size of the elementary cell.
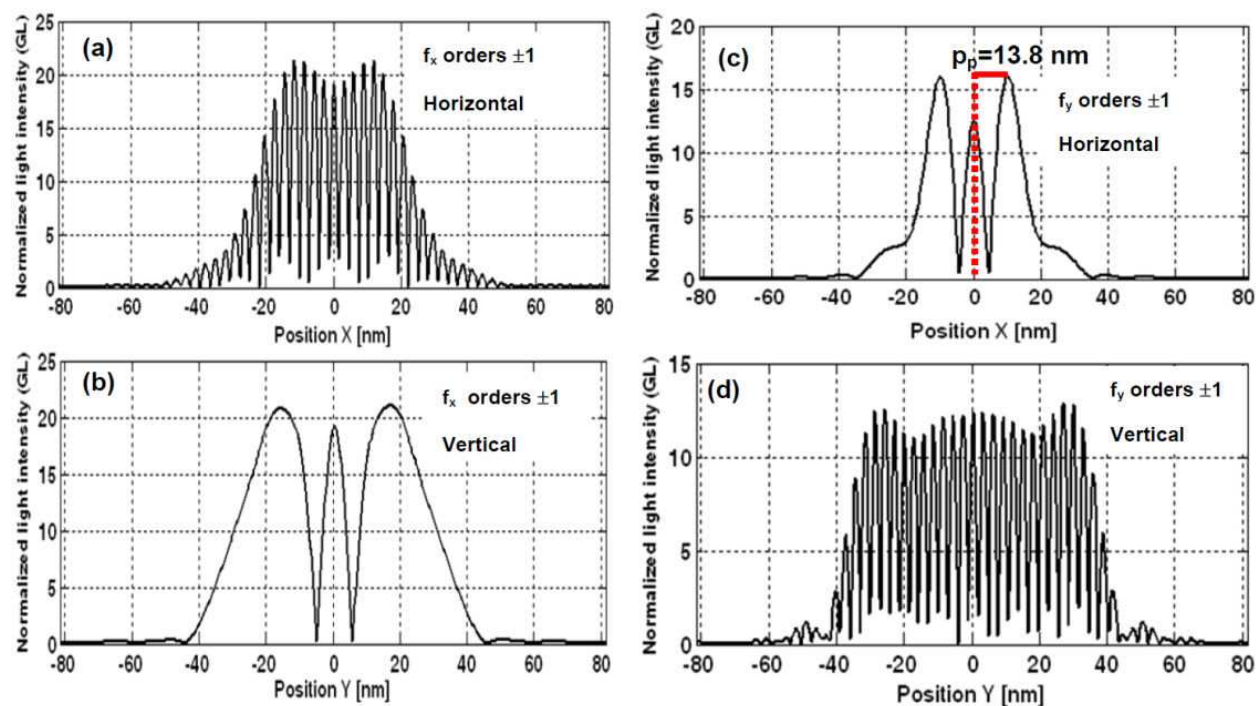

Figure 20. (a) Cross-section in the horizontal direction of the filtered pattern shown in Figure 19c (i.e. that obtained by selecting f_x-orders ±1); (b) Cross-section in the vertical direction of the filtered pattern of Figure 19c; (c) Cross-section in the horizontal direction of the filtered pattern shown in Figure 19d (i.e. that obtained by selecting f_y-orders ±1); (d) Cross-section along the vertical direction of the filtered pattern of Figure 19d.
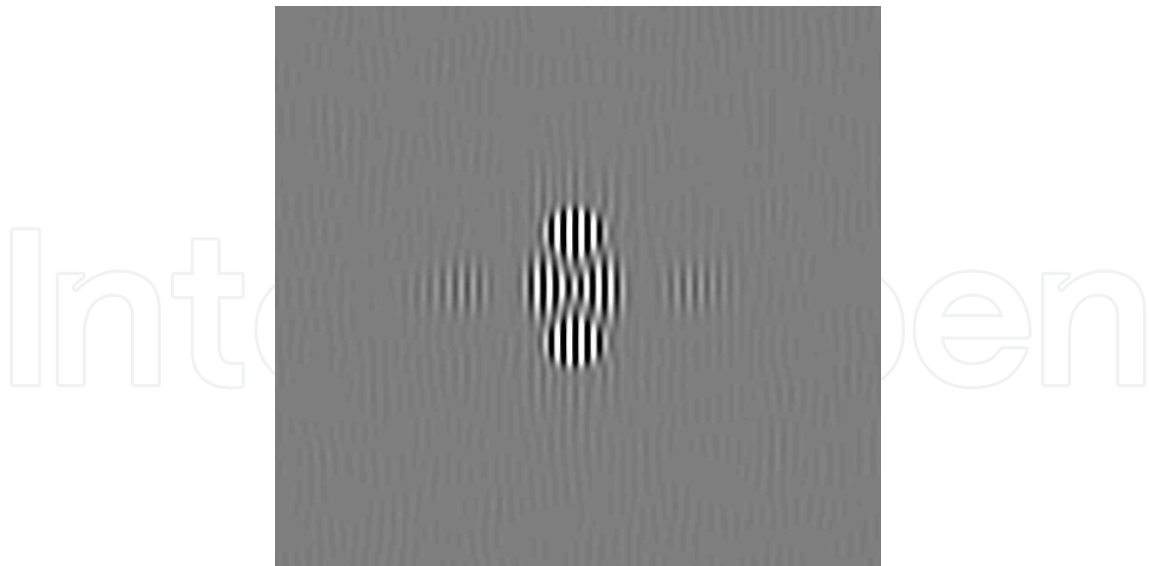
Figure 21. Result of the same processing operations utilized for the 86 nm nano-crystal actual image and then applied to the numerically reconstructed image pattern shown in Figure 17a.

If the same processing sequence utilized for the actual image recorded by the CCD sensor is applied to the simulated image, one regains the same structure of the inverse FT (see Figure 21). This indicates that the components are connected to the square shape of the cross-section of the nano-crystal and to the shifts between the 0 and the ±1 orders, which in turns are determined by the vibration mode of the crystal. The vibration mode of the nano-crystal is directly related to the diffraction pattern of the nano-crystal.
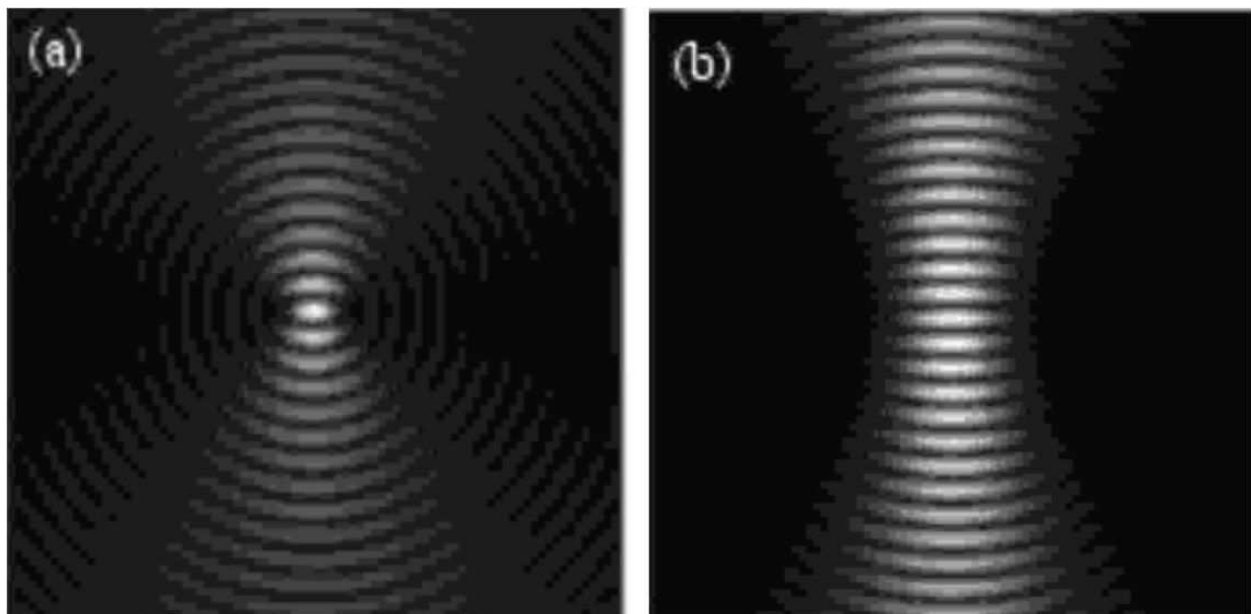

Figure 22. Transverse intensity profiles of non-diffracting Mathieu beams obtained for different values of wave solution parameters [20].

The obtained intensity profiles are similar to the intensity profiles of Mathieu non-diffract-ing wave fronts simulated in [20] (see Figure 22). The preceding analysis provides a strong evidence that the adopted models for the observed phenomena are supported by the analy-sis of the structure of the recorded images.

The assumption made in the "*Diffraction patterns of the observed objects*" section that the re-corded images are diffraction patterns of the NaCl nano-crystals is validated by all the mate-rial presented in the analysis of the images of the nano-crystals. Since the observed nano-crystals lay in the vertex plane normal to the optical axis of the spherical relay lens, following the classical interpretation given in FT optics one would say that the observed in-tensity distribution in the focal plane of the lens is the FT of the intensity distribution in the vertex plane. Although this concept corresponds to a two dimensional transparency (X-Y) intensity distribution, it is commonly extended to the case of thin objects located in the ver-tex plane. If one adds a reference point source in same plane of the object or a plane refer-ence wave front, the resulting intensity in the focal plane of the lens is called a FT hologram.

In the measurements discussed in this chapter, there is a difference with respect to classical FT holography: the diffraction pattern of the observed object is not the FT of the field distri-bution of the observed objects. The formation of the diffraction pattern obeys to different equations than those of the classical case. However, the final result is the same: one gets a hologram containing the diffraction pattern of the observed objects. Actually, because of the presence of many reference plane wave fronts, it corresponds to the Tanner [26] type of holograms of transparent objects. Hence, we are in presence of a different kind of hologram but that from the point of view of application has the same final result: it provides informa-tion on the geometrical configuration and optical properties of the observed object. These holograms share a common feature with classical FT holograms: they are formed by the dif-fraction pattern of the observed objects. The difference between the two types of holograms is that the diffraction pattern produced by the evanescent illumination is not a FT of the elec-tromagnetic field of the observed object.

11. Observation of the polystyrene nano-spheres

The preceding sections described the different aspects involved in the retrieval of the infor-mation concerning the geometry of isomers of NaCl nano-crystals. However, the analyzed images contain other objects besides NaCl nano-crystals: among these objects, nano-spheres are investigated.

Micro/nano-spheres made of transparent dielectric media are excellent optical resonators. Unlike the NaCl nano-crystals whose resonant modes to our knowledge have never been analyzed in the literature, both theoretical and experimental studies on the resonant modes of micro/nano-spheres are available in the literature. Of particular interest are the modes lo-calized on the surface of the sphere, along a thin ring located on the equator. These modes are called *whispering gallery modes* (WGM). WGM result from light confinement due to total internal reflection inside a high index spherical surface immersed in a lower index medium

and from resonance as the light travels a round trip within the cavity with phase matching [27]. The WG modes are included in the Mie's family of solutions for resonant modes in light scattering by dielectric spheres. The WG modes can be also derived from Maxwell's equations by imposing adequate boundary conditions [28]. WG modes can also be obtained as solutions of the Quantum Mechanics Schrodinger-like equation describing the evolution of a complex angular-momentum of a particle in a potential well (see, for example, references [29, 30] and the other references cited therein).

Figure 23a shows the image of a spherical nano-particle of diameter 150 nm. This image presents the typical whispering gallery mode intensity distribution. Waves are propagating around the diameter in opposite directions thus producing a standing wave with seven nodes and six maxima. The light is trapped inside the particle and there is basically a surface wave that only penetrates a small amount into the radial direction.
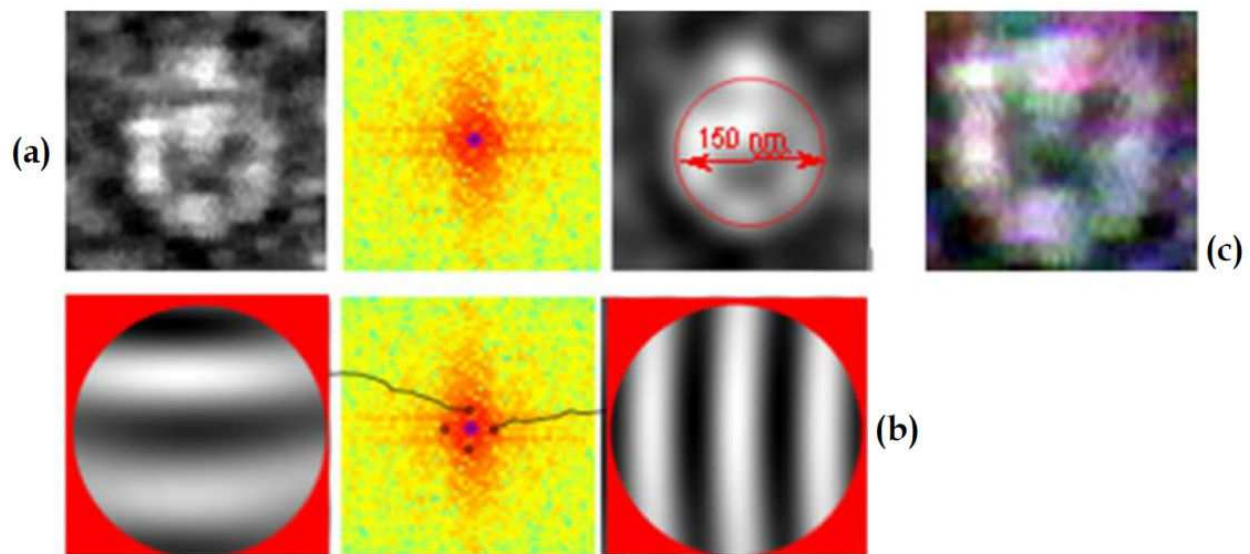

Figure 23. Spherical nano-particle of estimated diameter 150 nm: (a) FT and zero order filtered pattern; (b) Systems of fringes modulated by the particle; (c) Color image of the particle.

Similarly to the case of nano-crystals, the observed images are diffraction patterns of the electromagnetic field and are not actual images of the resonant modes of the spheres. As it can be seen in the images, different diffraction orders are present in the recorded images thus creating an effect that looks similar to an out-of-focus image. However, the changes between maxima and minima are preserved and can be utilized to ascertain the characteristics of the WG mode. As it occurs with the nano-crystals, the edges of the sphere image can be detected and analyzed.

The method of depth determination utilized for the nano-crystals can be applied also to the nano-spheres. While in prismatic bodies made out of plane surfaces the pattern interpretation is straightforward, in the case of curved surfaces the analysis of the patterns is more complex since light beams experience changes in trajectories determined by the laws of refraction. In the case of a sphere, the analysis of the patterns can be performed in a way simi-

lar to what is done in the analysis of the Ronchi test for lens aberrations. Figure 23b shows the distortion of a grating of pitch 83.4 nm that passes through the nano-sphere. The appearance of the observed fringes is similar to that observed in a Ronchi test. Through this analysis, the radius of curvature of the sphere is derived to be equal to 150 nm. The detailed description of this process is not included in this chapter for the sake of brevity.
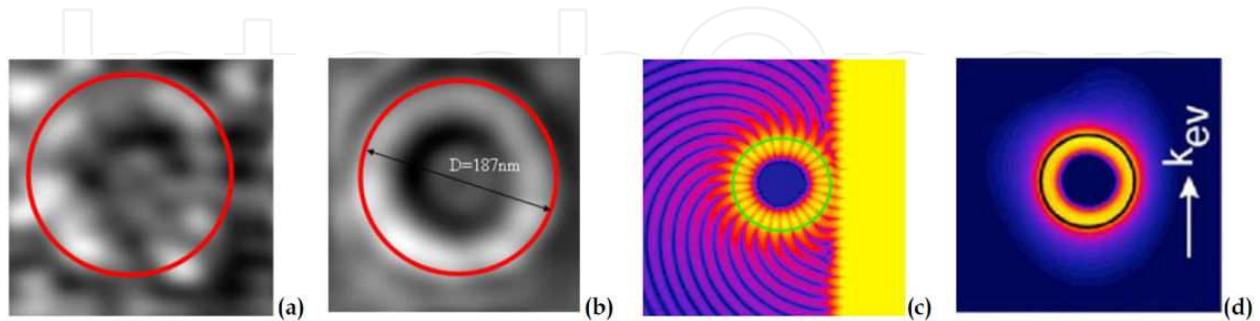

Figure 24. Spherical nano-particle of estimated diameter 187 nm and numerical simulations: (a) Original image; (b) Average intensity image; (c) Numerical simulation of whispering gallery modes [31]; (d) Average intensity of numerical simulation represented in Figure 24c.

Figure 24 shows a spherical particle of diameter 187 nm. The diameter has been obtained from the average intensity shown in Figure 24b. Figure 24c is taken from Ref. [31]. In [31], the WGM of a polystyrene microsphere of diameter 1.4 µm has been determined numerically. Figure 24c shows the pattern of the intensity of the electromagnetic field for the sphere equator. The average intensity corresponding to Figure 24c is represented in Figure 24d. The black circle included in Figure 24d corresponds to the green contour shown in Figure 24c that represents the surface of the microsphere. This boundary line also corresponds to the red line sketched in Figure 24b. In both cases, the field extends beyond the boundary of the sphere equator. There is a very good agreement between the experimental results and the numerical simulation. The electromagnetic resonance occurs at the wavelength λ=386 nm which corresponds to UV radiation. The color camera sensor is sensitive to this frequency and Figure 23c shows the color picture of the D=150 nm nano-sphere. Both the observed sphere and the sphere analyzed in the numerical example are made of polystyrene which has a resonance peak at the wavelength λ=386 nm.

The same procedure to determine geometry and shape applied to the nano-crystals has been applied to four spheres with radius ranging between 150 and 228 nm. For example, Figure 25 illustrates the different steps of the process for the 150 nm diameter particle shown in Figure 23a. The Fourier transform of the image is shown in Figure 25a. Figure 25b shows the Fourier transform of the real part of the FT of the image. Figure 25c presents the intensity distribution of the inverse transform of the filtered zero order shown in Figure 25b. Figure 25d and Figure 25e show the cross-sections of Figure 25c, respectively, in the X- and Y-directions. The structure of the zero order is complex. The gray level intensity decays from 255 to 20 within 75 nm: this quantity corresponds to the radius of the nano-sphere.
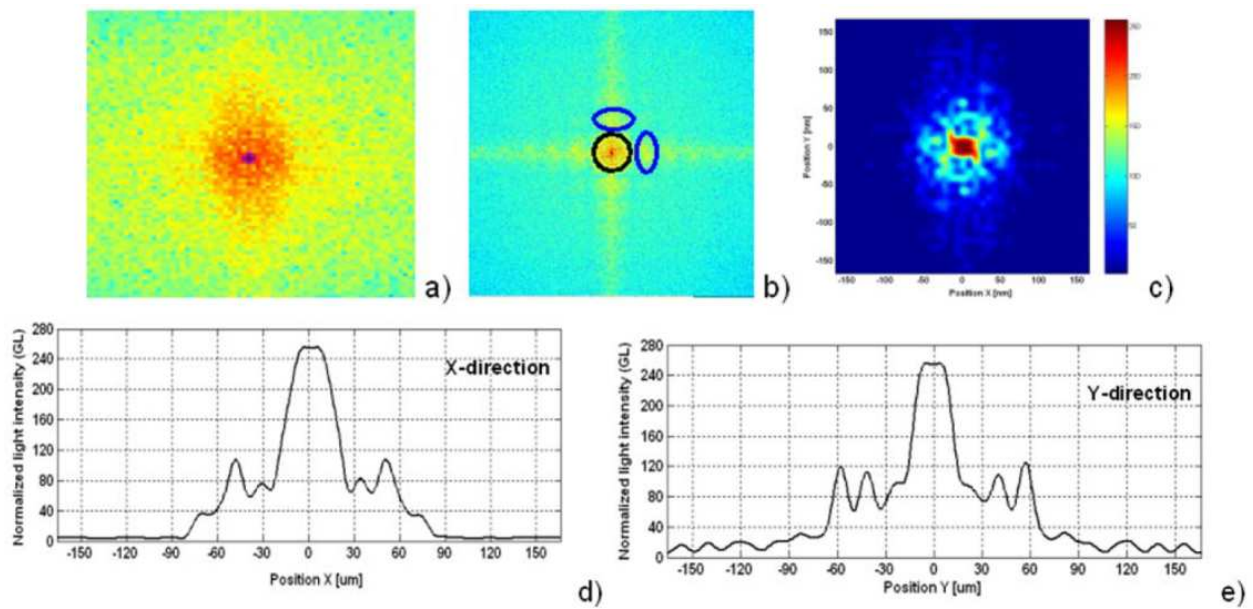
Figure 25. a) FT pattern of the image of the 150 nm polystyrene nano-sphere shown in Figure 23a; (b) Fourier transform of the real part of the FT of the nano-sphere; (c) 2-D view of the filtered zero order extracted from the real part of the FT pattern of the nano-sphere; (d) Cross-section of the filtered zero order in the X-direction; e) Cross-section of the filtered zero order in the Y-direction.
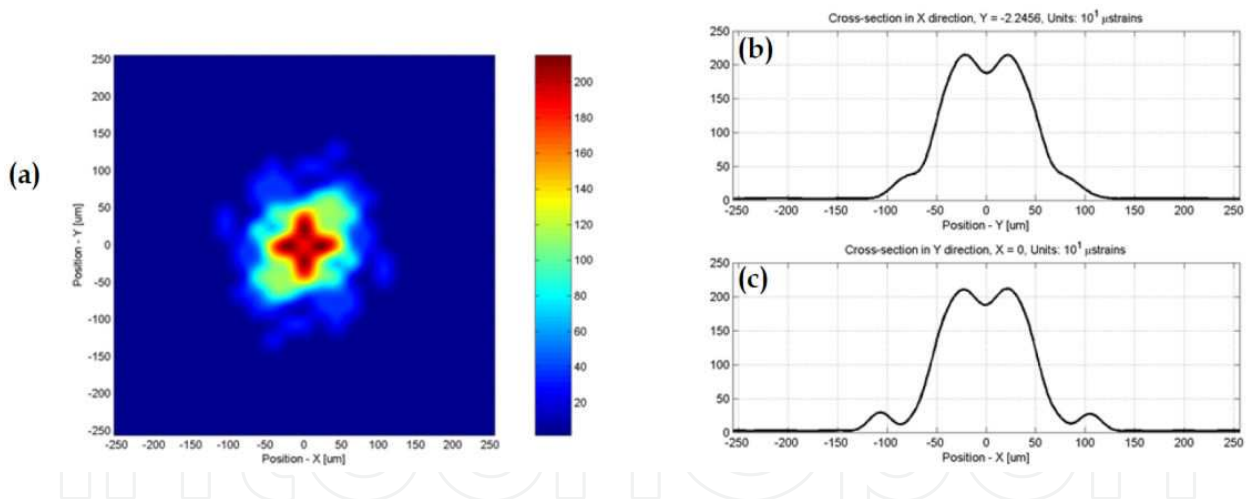

Figure 26. a) 2-D view of the filtered zero order extracted from the real part of the FT pattern of the polystyrene nano-sphere of diameter 187 nm shown in Figure 24a; (b) Cross-section of the filtered zero order in the X-direction; (c) Cross-section of the filtered zero order in the Y-direction.

The filtered zero order extracted from the real part of the FT pattern of the nano-sphere of diameter 187 nm is shown in Figure 26a. The structure of the order is far more symmetric than for the 150 nm diameter particle previously analyzed. Figures 26b-c show the cross-sections in the X and Y-directions of the filtered zero order, respectively. As in the preceding example, the intensity level drops sharply at the boundary of the equatorial region outlining the diameter of the sphere.
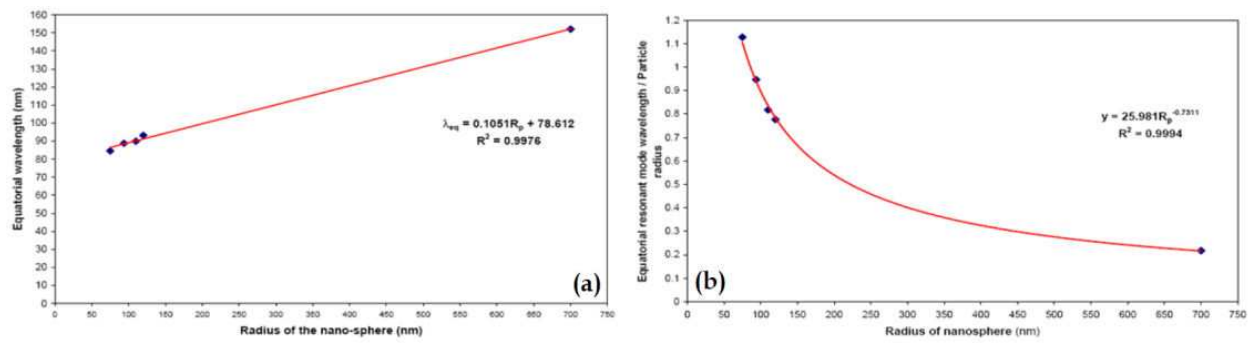
Figure 27. Relationships between nano-sphere radius and (a) equatorial wavelength of the WGM, (b) normalized equatorial wavelength of the WGM.

In order to verify that the pattern interpretation is in agreement with the presence of WGM modes, the experimentally determined equatorial wavelength of the WGM mode has been correlated with the sphere radius. Numerical results given in reference [31] also are included in the correlation. Two alternative correlation parameters have been considered following [32]. Figure 27a shows the variation of the equatorial wavelength vs. the radius of the sphere. Figure 27b shows the variation of the equatorial wavelength divided by the sphere radius vs. the sphere radius. Both models show a very high correlation coefficient R^2.

12. Numerical issues involved in the reconstruction process of nano-objects

There is a very important point to be made concerning the process of elaboration of the optically recorded data. The final results are a consequence of both optical and numerical super-resolution techniques [33]. These procedures have their foundations in two basic theorems of analytic functions. The FT of the images of nano-objects extended to the complex plane are analytical functions. If the FT of a function is known in a region of the domain under analysis, then, by analytic continuation the FT can be extended to the entire domain. The resolution obtained in this process is determined by the frequencies f_{sc} contained in the captured image. The images can be reconstructed by a combination of phase retrieval and suitable algorithms. The images can be reconstructed from a FT such that, if we call f_{sc} the maximum frequency that has been retrieved and $f_{sc,max}$ the maximum frequency content of the image, $f_{sc} \leq f_{sc,max}$.

The bi-cubical interpolation of pixels is a standard procedure utilized also in numerical super-resolution that allows getting sub-pixel resolutions. Furthermore, the fact that the process of image formation includes different replications of the image due to the different diffraction orders present in the image is an additional factor that increases the amount of information contained in an image. The effect of the successive images depends on the structure of the image plane array of the CCD, that is on the factor of fullness of the detector array, but it is equivalent to micro-scanning, which is to obtain successive frames of displaced

images. Finer sampling procedures produce higher accuracies and better modulation transfer functions (MTF) together with higher Nyquist frequencies [34].

13. Summary and conclusions

This chapter presented a new method to analyze the near field super-oscillatory field generated by evanescent illumination at the nano-scale by imaging the near field in the far field. This approach was successfully applied to measure the topography of nano-sized simple objects such as prismatic sodium-chloride crystals and spherical polystyrene particles. The obtained results are supported by additional experimental evidence that independently provides confirmation of the different applied procedures and adopted models.

The recorded images are nano-sized lens holograms of the diffraction patterns of the observed objects. In a manner of speaking, they are similar to FT holograms that are also lens holograms of the diffraction patterns of the observed objects but the process of formation of the diffraction patterns follows very different mechanisms. While the FT holograms are the result of illuminating the observed object with an external source, the diffraction of the observed objects in the proposed method is a consequence of self illumination caused by electromagnetic resonance produced by the electromagnetic field generated by multiple evanescent fields. The wave fronts that contain the diffraction patterns of the observed objects are solitons solutions of the Maxwell equations that are generated by the presence of a relay lens that converts the local super-oscillations in non-diffracting Bessel waves that to go through the whole process of image formation without the restrictions imposed by diffraction-limited optical instruments.

The degree of accuracy achieved in measurements is ascertained on the basis of the observed sodium-chloride nano-crystals. The actual sizes of the observed crystals are known from theoretical and independent experimental verifications [23]. The actual measured values and the error analysis of the obtained results can be found in [19]. Two types of correlation are established, one correlation corresponds to the theoretically formulated proportion rations of the nano-crystal contained in [23]. The mean error of the measured aspects ratios is 4.6% with a standard deviation of ±6.6%. The other correlation corresponds to the actual dimensions of the nano-crystals. The mean absolute error in the length measurements is of the order of 3 nm and the standard deviation is ±3.7 nm. The measured lengths of the crystals agree very well with the lengths computed from the sodium-chloride elementary cell size (d=0.573 nm at room temperature). The overall measurements performed show an overall standard deviation that is of the order of ±5 elementary cells.

In the case of the nano-spheres, trends of variation of the observed equatorial wavelength of the confined photons with respect to particle radius are in good agreement with numerical results reported in the literature.

The developed methodology is an effective tool to perform with visible light measurements in the nano-range in the far field with a traditional optical microscope thus overcoming the diffraction-limited resolution of optical microscopes that currently limits their use.

Author details

Cesar A. Sciammarella[1*], Luciano Lamberti[2] and Federico M. Sciammarella[1]

*Address all correspondence to: csciammarella@niu.edu

1 College of Engineering & Engineering Technology, Northern Illinois University, DeKalb, USA

2 Dipartimento di Meccanica, Matematica e Mananagement, Politecnico di Bari, Bari, Italy

References

[1]   Toraldo di Francia G. Super-gain antennas and optical resolving power. *Nuovo Cimento* 1952; 9(S3): 426-435.

[2]   Sciammarella CA, Lamberti L. Optical detection of information at the sub-wavelength level. In: *Proceedings of the* NANOMEC06 *Symposium on Materials Science and Materials Mechanics at the Nanoscale. Modeling, Experimental Mechanics & Applications*, November 2006, Bari, Italy.

[3]   Berry MV. Evanescent and real waves in quantum billiards and Gaussian beams. *Journal of Physics A: Mathematical and General* 1994; 27: 391-398.

[4]   Girard C, Dereux A, Martin OJF, Devel M. Generation of optical standing waves around mesoscopic surface structures: scattering and light confinement. *Physical Review B* 1995; 52(4): 2889-2898.

[5]   Toraldo di Francia G. *La Diffrazione della Luce*. Torino (Italy): Edizioni Scientifiche Einaudi; 1958. (In Italian)

[6]   Vigoureux JM. De l'onde évanescente de Fresnel au champ proche optique. *Annales de la Fondation Luis de Broglie* 2003; 28(3-4): 525-548.

[7]   Papoulis A. *The Fourier Integral and Its Applications*. New York (USA): McGraw-Hill; 1962.

[8]   General Stress Optics Inc. *Holo-Moiré Strain Analyzer (Holostrain) Version 2.0*, Chicago (USA), 2007. http://www.stressoptics.com.

[9]   Sciammarella CA, Lamberti L. Observation of fundamental variables of optical techniques in the nanometric range. In: Gdoutos EE (Ed) *Experimental Analysis of Nano and Engineering Materials and Structures*. Springer (The Netherlands); 2007. ISBN 978-1402062384

[10] Sciammarella CA, Lamberti L, Sciammarella FM. Light generation at the nano-scale, key to interferometry at the nano-scale. In: Proulx T. (Ed) *Conference Proceedings of the*

Society for Experimental Mechanics Series; Experimental and Applied Mechanics 6: 103-115. New York (USA): Springer; 2010. ISSN: 2191-5644.

[11] van de Hulst HC. *Light Scattering by Small Particles*, 2nd Edition. Mineola (USA): Courier Dover Publications; 1981.

[12] Guillemet C, Aclocque P. *Compte Rendue du Colloque sur la nature des surfaces vitreuses polies*. Charleroi (Belgium): Union Scientifique Continentale du Verre; pp. 121-134; (1959).

[13] Acloque P, Guillemet C. *Comptes Rendues de la Academie des Sciences* 1960; 250: 4328-4330.

[14] Ansevin RW. *Non Destructive Measurement of Surface Stresses in Glass*. Pittsburgh Plate Glass Company, Glass Research Center, Pittsburgh (USA), 1964.

[15] Guillemet C. *L'Interférométrie à Ondes Multiples Appliquée à Détermination de la Répartition de l'Indice de Réfraction Dans Un Milieu Stratifié*. PhD Dissertation, University of Paris. Paris (France): Imprimerie Jouve; 1970. (In French)

[16] Sciammarella CA. Experimental mechanics at the nanometric level. *Strain* 2008; 44(1): 3-19.

[17] Sciammarella CA, Lamberti L, Sciammarella FM. Optical holography reconstruction of nano-objects. In: Rosen J. (Ed.) *Holography, Research and Technologies*. Rijeka (HR): InTech; 2011. p191-216

[18] Ayyagari RS, Nair S. Scattering of P-polarized evanescent waves by a spherical dielectric particle. *Journal of the Optical Society of America, Part B: Optical Physics* 2009; 26(11): 2054-2058.

[19] Sciammarella CA, Lamberti L, Sciammarella FM. The equivalent of Fourier holography at the nanoscale. *Experimental Mechanics* 2009; 49(6): 747-773.

[20] Bouchal Z. Non diffracting optical beams: physical properties, experiments, and applications. *Czechoslovak Journal of Physics* 2003; 53(7): 537-578.

[21] Wang H, Shi LP, Lukyanchuk BS, Sheppard CJR, Chong TC, Yuan GQ. Super-resolution and non-diffraction longitudinal polarized beam, 2007. http://arxiv.org/ftp/arxiv/papers/0709/0709.2748.pdf (Accessed 16 August 2012)

[22] Wang H, Shi LP, Lukyanchuck BS, Sheppard CJR, Chong TW. Creation of a needle of longitudinally polarized light in vacuum using binary optics. *Nature Photonics* 2008; 2: 501-505.

[23] Hudgins RR, Dugourd P, Tenenbaum JN, Jarrold MF. Structural transitions of sodium nanocrystals. *Physical Review Letters* 1997; 78: 4213-4216.

[24] Burch JW, Gates C, Hall RGN, Tanner LH. Holography with a scatter-plate as a beam splitter and a pulsed ruby laser as light source. *Nature* 1966; 212: 1347-1348.

[25] Spencer RC, Anthony SAT. Real time holographic moiré patterns for flow visualization. *Applied Optics* 1968; 7(3): 561-561.

[26] Tanner LH. The scope and limitations of three-dimensional holography of phase objects. *Journal of Scientific Instruments* 1966; 44(12): 774-776.

[27] Johnson BR. Theory of morphology-dependent resonances - shape resonances and width formulas. *Journal of the Optical Society of America, Part A: Optics Image Science and Vision* 1993; 10(2): 343-352.

[28] Bohren CF, Huffman DR. *Absorption and Scattering of Light by Small Particles*. New York (USA): Wiley; 1998.

[29] Fan X, Doran A, Wang H. High-Q whispering gallery modes from a composite system of GaAs quantum well and fused silica microsphere. *Applied Physics Letters* 1998; 73(22): 3190-3192.

[30] Shopova SI. *Nanoparticle-Coated Optical Microresonators for Whispering-Gallery Lasing and Other Applications*. PhD Dissertation, Oklahoma State University, Stillwater (USA), 2007.

[31] Pack A. *Current Topics in Nano-Optics*. PhD Dissertation, Chemnitz Technical University, Chemnitz (Germany), 2001.

[32] Collot L, Lefèvre-Seguin V, Brune M, Raimond JM, Haroche S. Very High-Q Whispering-Gallery Mode resonances observed on fused silica microspheres. *Europhysics Letters* 1993; 23(5): 327-334.

[33] Borman S, Stevenson R. *Spatial Resolution Enhancement of Low Resolution Image Sequences, a Comprehensive Review with Directions for Future Research.* Laboratory for Image and Signal Analysis, IM 46556, University of Notredame (USA), 1998

[34] Boreman GD. *Modulation Transfer Function in Optical and Electro-Optical Systems.* Bellingham (USA): SPIE Press; 2001.